Compression stress–strain and creep properties of the 52In–48Sn and 97In–3Ag low-temperature Pb-free solders

Paul T. Vianco · Jerome A. Rejent · Arlo F. Fossum · Michael K. Neilsen

Published online: 23 September 2006
© Springer Science+Business Media, LLC 2006

Abstract Lead (Pb)-free, low melting temperature solders are required for step-soldering processes used to assemble micro-electrical mechanical system (MEMS) and optoelectronic (OE) devices. Stress–strain and creep studies, which provide solder mechanical properties for unified creep-plasticity (UCP) predictive models, were performed on the Pb-free 97In–3Ag (wt.%) and 58In–42Sn solders and counterpart Pb-bearing 80In–15Pb–5Ag and 70In–15Sn–9.6Pb–5.4Cd alloys. Stress–strain tests were performed at 4.4×10^{-5} s^{-1} and 8.8×10^{-4} s^{-1}. Stress–strain and creep tests were performed at –25, 25, 75, and 100°C or 125°C. The samples were evaluated in the as-fabricated and post-annealed conditions. The In–Ag solder had yield stress values of 0.5–8.5 MPa. The values of ΔH for steady-state creep were 99 ± 14 kJ/mol and 46 ± 11 kJ/mol, indicating that bulk diffusion controlled creep in the as-fabricated samples (former) and fast-diffusion controlled creep in the annealed samples (latter). The In–Sn yield stresses were 1.0–22 MPa and were not dependent on an annealed condition. The steady-state creep ΔH values were 55 ± 11 kJ/mol and 48 ± 13 kJ/mol for the as-fabricated and annealed samples, respectively, indicating the fast-diffusion controlled creep for the two conditions. The UCP constitutive models were derived for the In–Ag solder in the as-fabricated and annealed conditions.

Sandia is a multiprogram laboratory operated by Sandia Corporation, a Lockheed Martin Company, for the US Dept. of Energy's National Nuclear Security Administration under contract DE-AC04-94AL85000.

P. T. Vianco (✉) · J. A. Rejent · A. F. Fossum · M. K. Neilsen
Sandia National Laboratories, PO Box 5800, Albuquerque, NM 87185, USA
e-mail: ptvianc@sandia.gov

1 Introduction

Currently, the electronics industry is being tasked with developing lead (Pb)-free solders as alternatives to the traditional tin–lead (Sn–Pb) alloys for second-level (printed wiring assembly) interconnections. However, there are also applications that require lower temperature joining processes, which will also require Pb-free solders. For example, some high-valued, high-reliability military and space electronics are assembled with low-melting temperature solders simply to minimize damage to heat-sensitive components. On the other hand, there are complex assemblies that require low-temperature alloys as part of a multiple step-soldering process. In addition, circuitry constructed of precious metal conductors (e.g., hybrid microcircuits) use the low-temperature solders to avoid the rapid dissolution of conductor traces and pads that would occur with molten (Sn-based) solders that require higher process temperatures.

At present, there is a developing need for Pb-free, low-temperature soldering methods for advanced optoelectronic (OE), micro-electrical mechanical systems (MEMS), and micro-optical electrical mechanical system (MOEMS) devices. These products are highly complex, often having several devices in a single package, and as such, require multiple attachment steps. Also, a number of these components are

heat-sensitive, thereby requiring the use of low-temperature soldering processes.

Stringent package environments and device alignment requirements can be accommodated by the use of low-temperature, Pb-free solders in OE, MEMS, and MOEMS components. Low-temperature solders can reduce the temperature excursions required to assemble such packages. Also, they readily deform by creep, thereby reducing the residual stresses that can build up because of thermal expansion mismatches between joined structures. These residual stresses can give rise to the catastrophic failure of brittle components (e.g., GaAs laser diodes) immediately after assembly or generate misalignment between components later on, which degrades product performance in the field. Lastly, because solder joints are often essential for thermal management in OE packages, their integrity is critical towards the long-term reliability of several components (e.g., laser diodes).

Two low-melting temperature solders have been used rather extensively for a number of applications, including high-reliability printed circuit assemblies. Those materials, together with their respective solidus temperatures (T_s) and liquidus temperatures (T_l), are the 80In–15Pb–5Ag (wt.%) alloy, $T_s = 142°C$, $T_l = 149°C$; and the 70In–15Sn–9.6Pb–5.4Cd solder, $T_s = T_l = 125°C$. The compositions were abbreviated as In-Pb–Ag and In–Sn–Pb–Cd, respectively. These solders are particularly suited for Au-based conductors because the primary component, In, has a lower dissolution rate for Au than do Sn-based solders. Also, the In–Pb–Ag and In–Sn–Pb–Cd alloys exhibit excellent solderability and have provided the required service reliability.

Unfortunately, Cd and Pb have been targeted for elimination from electronic products. Therefore, Pb- and Cd-free alternative solders were sought for the In–Pb–Ag and In–Sn–Pb–Cd alloys. Based upon the need for similar liquidus and solidus temperatures, the two Pb-free solders, 97In–3Ag ($T_s = T_l = 143°C$) and 52In–48Sn ($T_s = T_l = 118°C$), were identified to replace the In–Pb–Ag and In–Sn–Pb–Cd alloys, respectively. Both alloys, which were abbreviated as In–Ag and In–Sn, respectively, are eutectic compositions [1].

The microstructures and primary phases of the In–Ag and In–Sn solders appear in Figs. 1 and 2, respectively. All samples were cooled at 10°C/min. The optical micrographs were digitally modified to enhance the second phase particles due to the difficulty with preparing In-based alloys for metallographic examination. In Fig. 1, the In–Ag alloy has a fine dispersion of very small $AgIn_2$ particles (light) within an essentially 100% In matrix (dark). The In–Sn alloy solidified

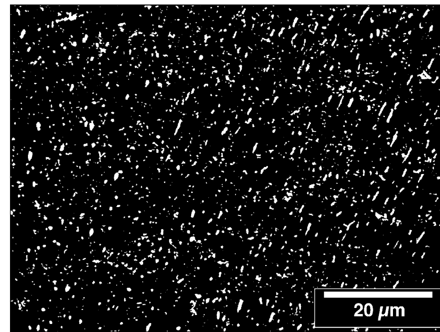

Fig. 1 Optical micrograph showing the In–Ag solder microstructure after solidification at 10°C/min. The image was digitally modified to enhance the light, Ag_3Sn particle phase against the darker, In-rich matrix phase

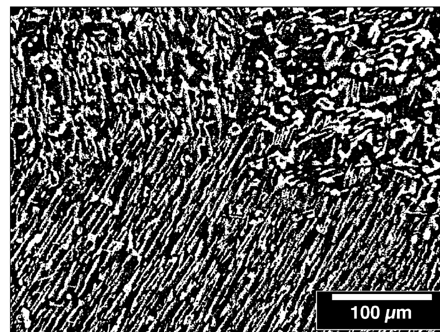

Fig. 2 Optical micrograph showing In–Sn solder microstructure after solidification at 10°C/min. The image was digitally modified to enhance the light, Sn-rich lamellae phase against the darker, In-rich matrix phase

into a more traditional lamellar microstructure. Each of the In-rich β phase (dark) and Sn-rich γ phase (light) had relatively high solubility limits for the other element—approximately 30 wt.% Sn and 23 wt.% In, respectively.

A second requirement of the candidate Pb-free solders was that they exhibit thermal mechanical fatigue (TMF) properties that were comparable to, or better than, those of the Pb- and Cd-bearing materials. Given the wide variety of potential applications of these solders in OE, MEMS, and MOEMS technologies, it became apparent that predicting the long-term reliability of the solder joints would require the use of computational models. Only through such models could the variety of solder joint geometries, substrate materials, and service environments be addressed in a timely and cost-effective manner. The basis of a TMF computational model is the unified creep-plasticity

(UCP) constitutive model that combines creep and plastic strain rates into a single inelastic strain rate. Experiments must be performed at a variety of temperatures and strain rates to obtain the material parameters for such models.

Several studies have investigated the mechanical properties of the low-temperature, Pb-free solders. Mei and Morris examined the creep behavior of 52In–48Sn alloy at temperatures of 20, 65, and 90°C, using a nine-solder joint, double-lap shear specimen [2]. The applied shear stresses ranged from 0.34 MPa to 6.9 MPa. The authors fitted the steady-state shear strain rate values, $d\gamma/dt$, to the power law (stress) expression $A\tau^n \exp(-\Delta H/RT)$ where A is a constant; τ is the applied shear stress; n is the power law exponent; ΔH is the apparent activation energy; R is the universal gas constant; and T is temperature. The values of A, n, and ΔH were $1.94 \times 10^4\ s^{-1}$, 3.2, and 96 kJ/mol, respectively. The relatively high ΔH value suggested that bulk diffusion was the active mechanism during creep.

Goldstein and Morris examined the shear stress–strain and creep behaviors of the 52In48Sn eutectic alloy using the double-lap shear (single joint) specimen [3]. The creep tests were performed at temperatures of 0–75°C. The shear stress–strain tests were performed at strain rates of $2 \times 10^{-4}\ s^{-1}$ to $8 \times 10^{-4}\ s^{-1}$; the creep tests used stresses from 1 MPa to 12 MPa. Shear yield stresses ranged from 7.8 MPa to 11.4 MPa between the respective strain rate limits, when tests were performed at 40°C. The stress–strain curves of these particular tests exhibited strain-softening plastic deformation. The creep parameters were determined according to the power law expression. The value of n was 3.3, which was very similar to that determined in [2]. The ΔH was 70 kJ/mol, which was less than the value obtained in that prior study, suggesting that a fast-diffusion process (e.g., grain boundary diffusion) contributed to creep deformation.

Hwang and Vargas examined the stress–strain and creep properties of the 60In–40Sn off-eutectic composition (T_s = 122°C, T_l = 118°C) using bulk tensile test samples [4]. The authors measured the room temperature 0.2% yield strength, ultimate tensile strength, and uniform elongation to be 4.6 MPa, 7.7 MPa, and 5.5%, respectively. (The authors did not note which of the two cited strain rates was used to collect that data: $8.8 \times 10^{-4}\ s^{-1}$ or $4.2 \times 10^{-3}\ s^{-1}$.)

The TMF performance of the In–Sn solder was documented with those of three other low-temperature solders in a study by Seyyed [5]. The test methodology was the thermal cycling of surface mount printed wiring assemblies. The strength of the gull-wing In–Sn solder joints exhibited a 75% decrease between 0 and 6,000 cycles (–10°C to 70°C; 1 min dwell; 20°C/min ramps). Similar behaviors were observed with the other low-temperature solders. The J-lead solder joint exhibited very little degradation for the In–Sn as well as the other solders. The strengths of the In–Sn solder joints were generally one-half the strengths of the baseline Sn–Pb solder joints.

It was concluded that there was insufficient stress–strain and creep data on the In–Sn or In–Ag alloys in the literature to develop the required UCP constitutive models. Therefore, a series of constant strain-rate, uniaxial stress–strain and creep compression experiments were performed on these Pb-free alloys. Parallel studies were also performed on the Pb-bearing counterparts, In–Pb–Ag and In–Sn–Pb–Cd, respectively. The yield stress and static elastic modulus were calculated from the true-stress, true-strain curves. The yield stress was also used to determine the applied stresses for the creep tests.

The quantitative metric of the creep tests was the *minimum creep rate*, $d\varepsilon/dt_{min}$, which characterizes the secondary or steady-state creep stage. Regardless of whether the exhaustion theory or the strain hardening theory governs primary creep, it has been proposed that similar deformation kinetics likely govern the two regimes [6–8]. Thus, the rate kinetics, which were based upon $d\varepsilon/dt_{min}$, could be used to predict both primary and secondary creep through the UCP constitutive model.

The UCP equation cannot address the tertiary creep stage. This stage, which is marked by an accelerating creep rate with time, results from the generation of cracks that quickly lead to creep rupture. Nevertheless, this study examined the strain–time curves for the onset of tertiary creep.

The physical metallurgy of the solders is an important facet of mechanical deformation. Microstructural features such as grain boundaries and dislocation structures determine the strain response of the material to the applied stress. Also, an understanding of the individual microstructures provides the means to more fully understand the stress–strain and creep behaviors of the solder. However, a detailed analysis of the physical metallurgy of the candidate solders was not performed in the current study. Solder microstructures were examined when there was the need to confirm tertiary creep behavior.

2 Experimental procedures

The solder compositions that were evaluated in this study were: 52In–48Sn (abbreviated as In–Sn),

70In–15Sn–9.6Pb–5.4Cd (In–Sn–Pb–Cd), 97In–3Ag (In–Ag), and 80In–15Pb–5Ag (In–Pb–Ag). All compositions were given in weight percent. Liquidus and solidus temperatures were cited in the Introduction section. The alloys were tested in the as-fabricated (i.e., as-cast) condition as well as after one of the three annealing treatments. The annealing temperatures were 52°C for the In–Sn and In–Sn–Pb–Cd solders, and 67°C for the In–Ag and In–Pb–Ag alloys. The annealing times were 8, 16, and 24 h. The temperature values were calculated, based upon approximately 82% of the solidus temperatures (K) from the two alloy groups. Imposing an annealing treatment prior to testing allowed for an evaluation of the effects that microstructural stabilization have on the mechanical properties.

The compression test method was used to collect stress–strain and creep data. The nominal dimensions of the cylindrical samples were 10 mm diameter and 19 mm length. The stress–strain tests were performed at one of two (engineering) strain rates: 4.4×10^{-5} s^{-1} or 8.8×10^{-4} s^{-1}. These relatively low values were selected to measure the deformation properties at strain rates that were commensurate with typical TMF conditions. The test temperatures were listed in Table 1 for each of the solder compositions. Duplicate samples were tested per each time, temperature, and annealing condition. Further details of the experimental procedures have been presented in previous publications [9, 10].

The stress–strain tests were analyzed to obtain the following properties: (1) yield stress, (2) static elastic modulus, and (3) yield strain. The yield strain data will not be reported here. Engineering stresses and strains were used to calculate the yield stress because they were suitable approximations to true stresses and true strains at these low strain values [11]. The yield stress was determined, using the 0.2% offset method [12]. Error terms were based upon scatter of the load–displacement curve at the intersection between the plot and the 0.2% intercept line.

The static elastic modulus was calculated from the linear portion of the stress–strain curve. A linear least-squares fit provided the slope (Δload/Δdisplacement). That slope value was multiplied by l_0/A_0 to determine the static elastic modulus, where l_0 and A_0 were the initial (gage) length and cross sectional area, respectively.

Table 1 Compression test temperatures used for each solder alloy composition

Solder	Test temperature (°C)
In–Sn	–25, 25, 75, 100
In–Sn–Pb–Cd	–25, 25, 75, 100
In–Ag	–25, 25, 75, 125
In–Pb–Ag	–25, 25, 75, 125

Lastly, the load–displacement plots were converted to true stress (σ) and true strain (ε) curves. The true stress and true strain values were calculated from the load–displacement data using Eqs. 1 and 2, respectively, shown below [11]:

$$\sigma = (L/\mathrm{A}_0)(\Delta l/l_0 + 1) = (L/A_0)(l/l_0) \quad (1)$$

$$\varepsilon = \ln(l/l_0) \quad (2)$$

Compression creep tests were performed, using the same test temperatures as listed in Table 1. The samples were tested in the as-fabricated condition or after annealing for 16 h at one of the two temperatures noted above. The initial applied stresses were identified from the yield stresses measured at the slower strain rate, 4.4×10^{-5} s^{-1}, per each of the test temperatures. Specifically, those stress values were 20%, 40%, 60%, and 80% of the mean yield stress measured between samples in both the as-fabricated and 16 h annealing condition. The stresses are listed in Table 2 as a function of test temperature.

The creep experiments were allowed to progress through the secondary or steady-state creep stage to determine the minimum creep rate, $\mathrm{d}\varepsilon/\mathrm{d}t_{\min}$. At very low stress for which, primary creep occurred over a longer time period, the test was concluded after approximately 3300 min (2.3 days). In such cases, the minimum creep rate was calculated from data taken at the end of the test. The parameters $\mathrm{d}\varepsilon/\mathrm{d}t_{\min}$ as well as the applied stress, σ, and temperature, T, were expressed by the sinh law creep equation (3) below:

$$\mathrm{d}\varepsilon/\mathrm{d}t_{\min} = f_0 \sinh^p(\alpha\sigma)\exp(-\Delta H/RT) \quad (3)$$

where f_0 is a constant (s^{-1}); p is the sinh term exponent (a constant also); α is the stress coefficient (MPa^{-1}); ΔH is the apparent activation energy (J/mol); R is the universal gas constant (8.314 J/mol-K) ; and T is the temperature (K). The applied stress was calculated from cross section of the deformed sample, using Eq. 1. The stress coefficient, α, is temperature dependent. However, its dependence was sufficiently weak such that it was considered a constant. (The product, $\alpha\sigma$, is often referred to as an *effective stress*.) The sinh law was selected because of its success for representing secondary creep deformation in metals and alloys, including solders, by avoiding the power law breakdown phenomenon encountered when attempting to use the simpler power law representation over a substantial stress range [13, 14].

Table 2 Compression creep stresses used for each temperature and solder alloy composition

Solder	Annealing conditions	Nominal stress (MPa)	Test temperature (°C)
In–Sn	52,°C, 16 h	3.3, 6.7, 10, 13	–25
		3.7, 5.6, 7.5	25
		0.86, 1.3, 1.7	75
		0.47, 0.71, 0.94	100
In–Sn–Pb–Cd	52°C, 16 h	5.4, 7.2, 11	–25
		2.7, 4.0, 5.4	25
		0.50, 0.70, 1.0	75
		0.27, 0.41, 0.55	100
In–Ag	67°C, 16 h	1.2, 2.3, 3.5, 4.6	–25
		0.75, 1.5, 2.3, 3.0	25
		0.84, 1.3, 1.7	75
		0.16, 0.33, 0.49, 0.65	125
In–Pb–Ag	67°C, 16 h	3.9, 7.8, 12, 16	–25
		1.9, 3.7, 5.6, 7.4	25
		0.50, 1.0, 1.5, 2.0	75
		0.13, 0.27, 0.40, 0.54	125

The values of f_0, Q/R, and p were calculated, using a multivariable, linear regression analysis that was performed on the logarithm of equation (3). The parameters $1/T$ and $\ln[\sinh(\alpha\sigma)]$ were the independent variables and $\ln(d\varepsilon/dt_{\min})$ was the dependent variable. The regression analysis was performed for different values of α . The value of α was selected, which maximized the square of the correlation coefficient, R^2, at the 95% confidence interval.

3 Results and discussion

3.1 In–Ag and In–Pb–Ag solders—compression stress–strain data

Shown in Fig. 3 are the true-stress, true-strain curves for the In–Ag solder. The plots represent the as-fabricated condition and the annealing treatment of 16 h at 67°C. The stress–strain curves, which corresponded to the other annealing times, were omitted for clarity as their trends were similar to those shown here. Both strain rates, 4.4×10^{-5} s^{-1} (a, b) and 8.8×10^{-4} s^{-1} (c, d) were represented in the plots. Under *all* conditions, work hardening was most significant at –25°C and then diminished with increased test temperature. At the slower strain rate of 4.4×10^{-5} s^{-1}, the as-fabricated (Fig. 3a) and annealed (Fig. 3b) conditions resulted in nearly identical stress–strain curves at each test temperature. At the faster strain rate of 4.4×10^{-5} s^{-1}, the extent of work hardening was slightly greater, as expected. Nevertheless, the as-fabricated samples (Fig. 3c) and annealed samples (Fig. 3d) exhibited similar degrees of work hardening.

Two general trends were observed in Fig. 3. First, the degree of work hardening decreased with increasing test temperature. This behavior resulted from dynamic recovery and recrystallization processes resulting from tests being performed at a high homologous temperature, T_h, where $T_h = T_{test}$ (K)/$T_{solidus}$ (K). The value of T_h was 0.60–0.96 for test temperatures in the range of –25 to 125°C. The second trend was the negligible effect of annealing treatment on the stress–strain curves. This behavior indicated that the In–Ag microstructure and responsible deformation mechanisms were not affected by the relatively ''impressive'' annealing conditions.

The yield stress was plotted as a function of annealing time in Fig. 4 for the In–Ag specimens tested at a strain rate of 4.4×10^{-5} s^{-1}. The open symbols were the mean values; the corresponding solid symbols were the minimum and maximum values. This plot illustrated three points: First of all, as expected, the yield stress decreased with increasing test temperature. Second, there was a relatively small scatter between the two yield stress measurements made per test condition. The same two trends were observed in the yield stress measured at the faster strain rate of 8.8×10^{-4} s^{-1}. Third, the effect of the annealing treatment time, which was to decrease the yield stress, was significant only at the 25 and –25°C test temperatures. At 25°C, the decrease of yield stress was observed only after the 24 h annealing treatment. At –25°C, both 16 and 24 h heat treatments caused a drop of yield stress. The 8 h heat treatment produced a slightly higher yield stress than the as-fabricated condition. However, the difference remained within experimental error. At the fast strain rate, annealing treatment produced a noticeable decrease of yield stress at 25 and –25°C, as well, but only following the 24 h period.

The entire set of *mean* yield stress values obtained for the In–Ag solder were plotted as a function of test temperature in Fig. 5. Overall, the yield stress values were in the range of 0.5–8.5 MPa and the plot shows

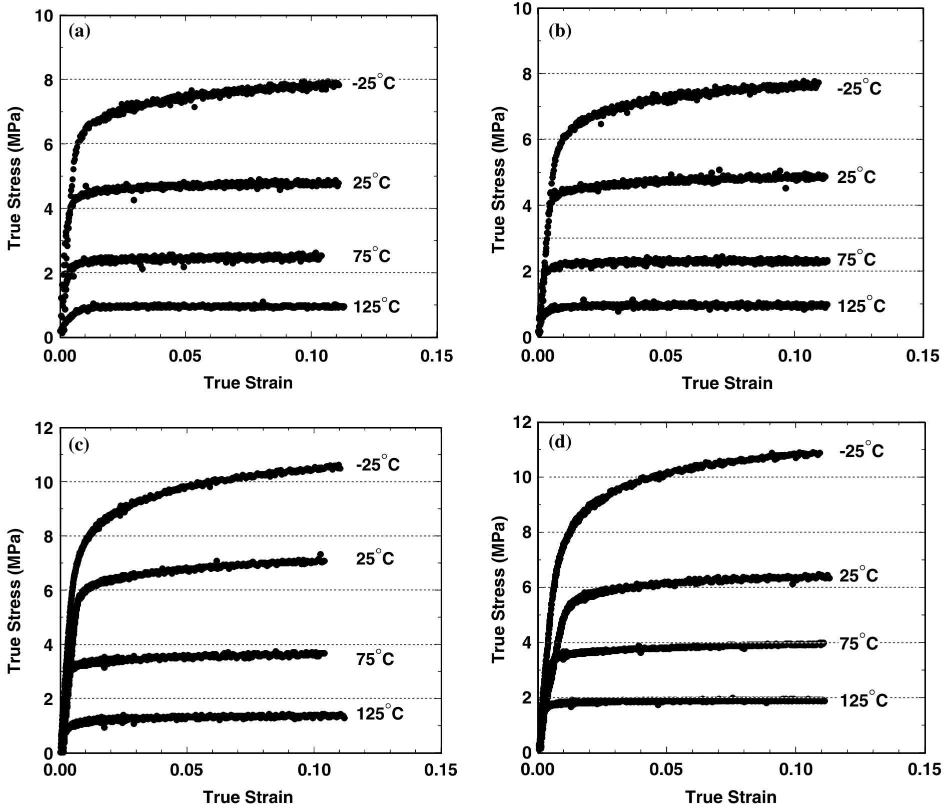

Fig. 3 Stress–strain curves for the In–Ag solder for the following combinations of sample condition and strain rate: (**a**) as-fabricated, $4.4 \times 10^{-5}\ s^{-1}$; (**b**) annealed (67°C, 16 h), $4.4 \times 10^{-5}\ s^{-1}$; (**c**) as-fabricated, $8.8 \times 10^{-4}\ s^{-1}$; and (**d**) annealed (67°C, 16 h), $8.8 \times 10^{-4}\ s^{-1}$

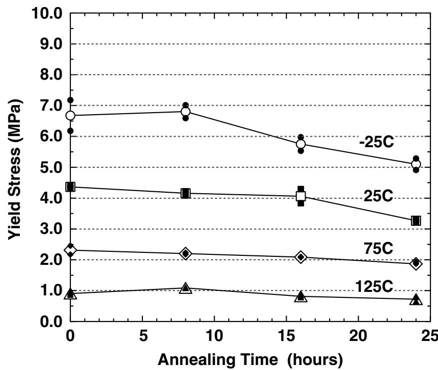

Fig. 4 Yield stress as a function of annealing time (67°C) for the In–Ag solder tested at a strain rate of $4.4 \times 10^{-5}\ s^{-1}$. The open symbols are the mean values; the corresponding solid symbols are the minimum and maximum values

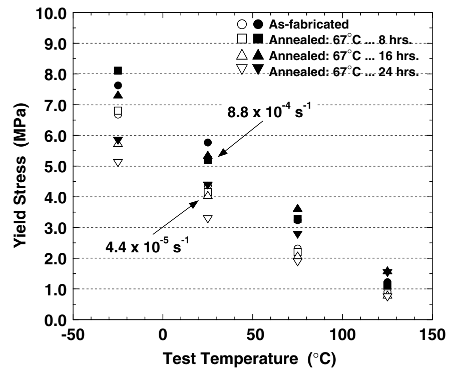

Fig. 5 Yield stress as a function of test temperature and annealing times (67°C) for the In–Ag solder. The open and closed symbols indicated the $4.4 \times 10^{-5}\ s^{-1}$ and the $8.8 \times 10^{-4}\ s^{-1}$ strain rates, respectively

the magnitude of the strain rate effect. Although the slower strain rate produced a lower yield stress, that difference became less significant with increased test temperature. The trends observed in Fig. 4, regarding the effects of annealing time on the yield stress at the slow strain rate, were also observed at the fast strain rate. In particular, there was the non-monotonic dependence of yield stress on annealing time at –25°C as well as the overall increasing insensitivity to annealing treatment with higher test temperatures.

In summary, the In–Ag solder exhibited the expected trends of decreasing yield stress with slower strain rates and increasing test temperature. Only the 16 and 24 h annealing times (67°C) caused noticeable changes of yield stress; moreover, those changes were limited to decreased values at only the 25 and –25°C test temperatures. This trend indicated that yield stress was most sensitive to the starting microstructure, as established by the annealing condition, at the lower test temperatures (–25 and 25°C). The strain rate effect became less distinct with increased testing temperature.

Understanding the above trends provided insight into the performance of the In–Ag solder in actual OE, MEMS, and MOEMS application, albeit to a limited degree because only the constant strain rate deformation has thus far been considered. In the foreseeable future, OE and MEMS devices will be exposed to service condition primarily in the low-temperature regime, in the present case, –25 to 25°C. As noted above, the stress–strain curves and, in particular, the yield stresses were most sensitive to the initial microstructure, as established by the annealing conditions in these experiments (or the process cooling rate in actual assemblies). The variability of the yield stress must be considered when constructing the UCP constitutive model, likely adding to the latter's complexity. The alternative approach is to define an ''average'' parameter and accept the possible loss of prediction fidelity.

The constant strain rate, uniaxial compression experiments were also evaluated for the counterpart Pb-bearing solder, In–Pb–Ag. At a strain rate of 4.4×10^{-5} s^{-1} and the as-fabricated condition, the In–Pb–Ag stress–strain curves exhibited work hardening only at –25°C. Work hardening was very minimal at 25°C. At 75°C or 125°C, the stress fluctuated with the progression of deformation. The stress varied by 0.3 MPa, peak-to-peak, over a strain ''period'' of 0.05 at 75°C, as shown in Fig. 6. The fluctuations diminished in magnitude at 125°C. At the faster strain rate of 8.8×10^{-4} s^{-1}, work hardening was recorded at –25 and 25°C and a monotonic strain-softening occurred at 75 and 125°C. The overall complex

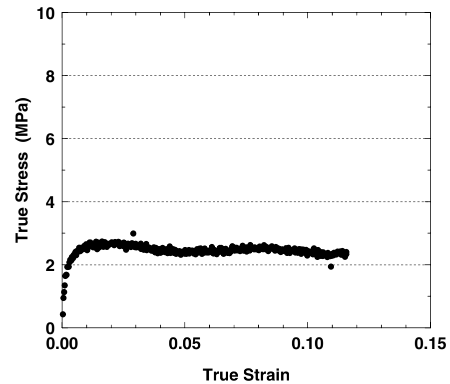

Fig. 6 Stress–strain curve for the as-cast In–Pb–Ag that was obtained at 75°C and a strain rate of 4.4×10^{-5} s^{-1} showing fluctuations of stress as a function of strain

stress–strain behavior of the In–Pb–Ag solder suggested that it had a less stable microstructure during deformation than did the In–Ag solder. Like the In–Ag solder, the annealing treatments had a minimal effect on the stress–strain curves.

The yield stress data were plotted in Fig. 7 for the In–Pb–Ag solder. The yield stress was in the range of 1.0–23 MPa, which was nearly twice that of the In–Ag solder (Fig. 5), indicating a greater temperature sensitivity. The majority of that difference between the two solders occurred at –25 and 25°C for either strain rate. The two solders exhibited comparable yield strengths at 75 and 125°C. At the faster strain rate of 8.8×10^{-4} s^{-1}, the In–Pb–Ag solder was stronger than the In–Ag solder at all test temperatures.

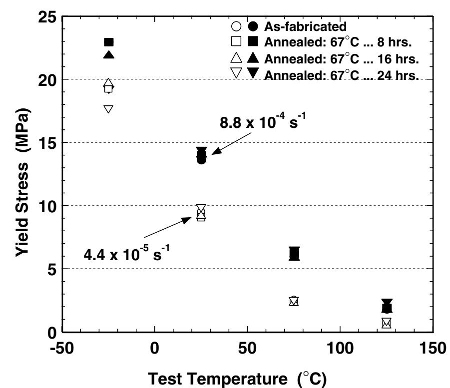

Fig. 7 Yield stress as a function of test temperature and annealing times (67°C) for the In–Pb–Ag solder. The open and closed symbols indicated the 4.4×10^{-5} s^{-1} and the 8.8×10^{-4} s^{-1} strain rates, respectively

The yield stress values of the In–Pb–Ag solder were even less sensitive to the annealing treatments than were those measured for the In–Ag solder. The 24 h heat treatment caused a significant strength decrease, but only at –25°C.

In summary, the yield stress of the In–Pb–Ag solder exhibited many of the same general trends as were noted for the In–Ag solder as a function of strain rate, test temperature, and annealing treatment. The differences rested primarily in the magnitudes of the effects. The In–Pb–Ag solder was generally stronger than the In–Ag solder, especially at the –25 and 25°C test temperatures. Because that difference diminished significantly at 75 and 125°C, the In–Pb–Ag solder yield stress had a greater sensitivity to test temperature than the In–Ag solder. On the other hand, the In–Pb–Ag solder exhibited a lesser sensitivity to the annealing treatment. If one were making a prediction of the ability of the In–Ag versus In–Pb–Ag to relieve residual stresses at low temperatures (< 75°C), based solely on a lower yield stress, it would appear that the In–Ag solder would be the better selection.

The static elastic modulus was determined from the initial, linear segment of the compression stress–strain curves. The linearity of that early portion of each curve was confirmed by the R^2 values of a linear regression analysis, which were rarely below 0.95. The static elastic moduli were plotted as a function of test temperature in Fig. 8 for the In–Ag solder. The strain rate was $4.4 \times 10^{-5}\ s^{-1}$. The samples were tested in the as-fabricated condition and following the annealing treatment for 24 h. The large symbols are the mean values; the smaller symbols are the individual measurements. The purpose of this figure was to demonstrate the scatter observed in these measurements. The scatter was greatest with the as-fabricated specimens and least with those annealed for 24 h. However, the scatter did not monotonically decrease for 8 and 16 h. The largest decrease in scatter occurred between the 16 h and 24 h time periods. Very similar trends were observed for samples tested at the faster strain rate of $8.8 \times 10^{-4}\ s^{-1}$. Therefore, variability of the static elastic modulus values indicated that the 24 h heat treatment was required to adequately stabilize the In–Ag microstructure.

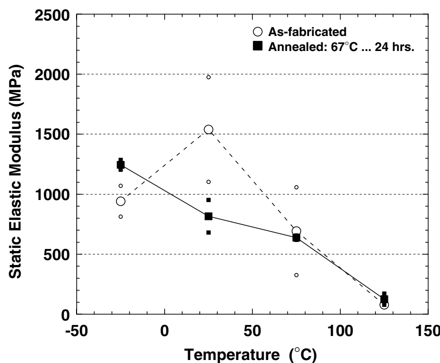

Fig. 8 Static elastic modulus as a function of test temperature for the In–Ag solder. The strain rate was $4.4 \times 10^{-5}\ s^{-1}$. The two sample conditions, as-fabricated and annealed at 24 h (67°C) were represented. The large symbols are the mean values; the smaller symbols are the two individual maximum and minimum points

It was observed in Fig. 8 that the static elastic modulus values were nearly an order of magnitude lower than those expected from solders or other metals and alloys [15]. The same behavior was observed in a study of the Sn–Ag–Cu solder [9]. In that study, an exhaustive assessment was made to determine whether the testing procedures were the source of the reduced moduli. Factors such as load train compliance as well as sample alignment and possible calculation errors were ruled out[1]. Therefore, it was concluded that the In–Ag solder exhibited either anelastic or significant inelastic deformation that accompanied the purely linear elastic response of the sample, at the initial, low stress portion of the stress–strain curve.

Unfortunately, existing UCP models assume that at low stress levels, the material response is linear elastic. These models do not account for any anelastic or significant inelastic strain at low stress levels. This model deficiency could have a significant negative impact on the accuracy of model predictions, especially in the present circumstance of the material being used at a high homologous temperature.

Next, the static modulus values of the In–Ag solder were examined as a function of test temperature and annealing time (67°C). The data were compiled in Fig. 9a for the slower strain rate of $4.4 \times 10^{-5}\ s^{-1}$. In the as-fabricated condition, the samples exhibited a maximum in the static elastic modulus at 25°C. This same behavior was observed for the stress–strain data of the Sn-Ag-Cu solder, using similar test parameters [9]. For those samples annealed for 8 and 16 h, a similar maximum was observed; but, it shifted to 75 and 125°C, respectively, albeit the latter case remained somewhat tentative in the absence of data beyond 125°C. A monotonically decreasing modulus was observed for those samples that were annealed for 24 h,

[1] Tests were preformed on Sn–Ag–Cu samples at considerably faster strain rates of up to $10^{-2}\ s^{-1}$ [16]. The static elastic moduli values had similar magnitudes.

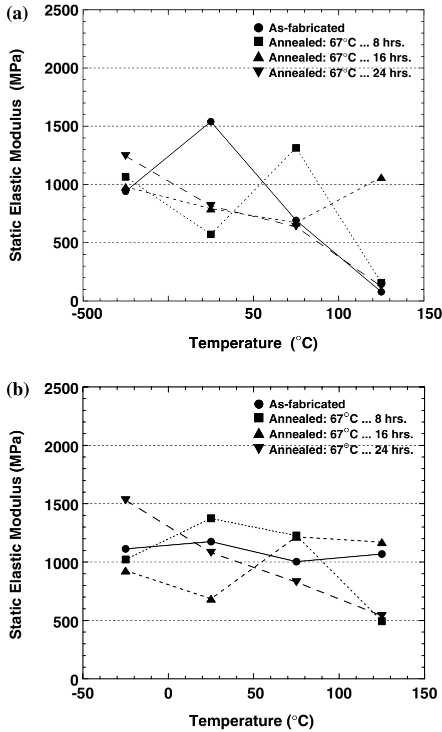

Fig. 9 Static elastic modulus (mean) as a function of test temperature for the In–Ag solder. The samples were in the as-fabricated condition as well as after having been annealed at 67°C for 8, 16, and 24 h. The two plots showed the moduli for the two strain rates (**a**) 4.4×10^{-5} s^{-1} and (**b**) 8.8×10^{-4} s^{-1}

implying that the maximum had been eliminated or moved to a temperature beyond the current test regime.

An analysis was also made of the In–Ag static elastic modulus values measured at the faster strain rate of 8.8×10^{-4} s^{-1}. The mean static elastic moduli were plotted as a function of test temperature and heat treatment in Fig. 9b. The values representing the as-fabricated condition fluctuated very little versus temperature when compared to the slower strain rate (Fig. 9a). The 8 h annealing treatment resulted in a maximum modulus between 25 and 75°C. The 16 h annealing treatment resulted in a general decrease of modulus with increasing test temperature, but with an apparent maximum at 75°C. A monotonically decreasing static elastic modulus was observed versus test temperature for samples annealed for 24 h prior to testing. However, the decrease was not as sharp as that observed at the slower strain rate.

The presence of an anelastic or inelastic deformation concurrent with the linear elastic deformation was further substantiated by the different behaviors observed between Fig. 9a and b. Although the strain rates differed by nearly an order of magnitude, such a difference would not be expected to affect either the magnitude, or the temperature dependence, of strictly the linear elastic modulus to the degree observed in the plots of Fig. 9.

In summary, the static elastic modulus was evaluated for the In–Ag solder. It was concluded that the unexpectedly low values (by nearly an order-of-magnitude) indicated that anelastic or inelastic deformation must have accompanied the expected linear elastic deformation in the stress–strain curve. The scatter of the modulus values, as well as their test temperature dependence, indicated that the 24 h annealing treatment (67°C) was required to provide some stability to the In–Ag microstructure, resulting in a monotonic decrease of modulus with increasing test temperature. Finally, the variations in the static elastic modulus would complicate UCP model development. ''Average'' static modulus values could be used in the constitutive equation to reduce model complexity, but with a potential loss of prediction fidelity.

The static elastic modulus values were similarly investigated for the In–Pb–Ag solder. Shown in Fig. 10 are the moduli measured at the slow strain rate of 4.4×10^{-5} s^{-1}. The samples were tested in the as-fabricated condition as well as after having been annealed for the longest interval of 24 h (67°C). When compared to similar data for the In–Ag solder (Fig. 8), the

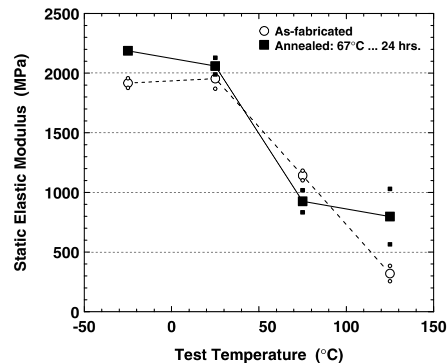

Fig. 10 Static elastic modulus as a function of test temperature for the In–Pb–Ag solder. The strain rate was 4.4×10^{-5} s^{-1}. The two sample conditions, as-fabricated and annealed at 24 h (67°C) were represented. The large symbols are the mean values; the smaller symbols are the two individual maximum and minimum points

In–Pb–Ag values exhibited slightly less scatter, particularly for the as-fabricated condition. At the intermediate heat treatments and faster strain rate, the In–Pb–Ag and In–Ag solders exhibited similar data scatter.

A comparison of Figs. 8 and 10 revealed several observations. First of all, the modulus values were higher for the In–Pb–Ag solder at each of the temperatures and both the as-fabricated and annealed conditions. The stiffness difference was particularly significant at the two lowest test temperatures of –25 and 25°C The higher modulus of the In–Pb–Ag solder placed this alloy at a disadvantage vis-à-vis the In–Ag solder in terms of its ability to relieve residual stresses caused by thermal expansion mismatch between materials in the joint, particularly at the low temperatures. This detriment is especially important in the low-temperature regime where creep mechanisms are ineffective at relieving residual stresses.

Although the In–Pb–Ag solder showed a general decrease of static elastic moduli with increased temperature, the values appeared to be segregated into two regimes: The high values at –25 and 25°C stepped down to the low values at 75 and 125°C. This behavior indicated that there was a transition in anelastic or inelastic deformation that occurred simultaneously with the linear elastic behavior. It was unlikely that there was a change to the linear elastic deformation because there were no phase changes reported to occur in this material over this temperature regime.

It was observed in Fig. 10 that static elastic modulus values of the In–Pb–Ag solder exhibited very little difference between the as-fabricated condition and the longest annealing time of 24 h (67°C). The absence of a consistent dependence of the static elastic modulus on annealing treatment was observed at both strain rates, as can be observed in Fig. 11a (4.4×10^{-5} s^{-1}) and 11b (8.8×10^{-4} s^{-1}). The static elastic moduli values were plotted as a function of test temperature. In Fig. 11a, the annealing times of 8 and 24 h indicated the step in the modulus values between 25°C and 75°C. The exception was the 16 h annealing treatment and, specifically, 25°C datum. This step behavior appeared to have shifted to the 75°C temperature at the faster strain rate (Fig. 11b). The different trends observed between the two strain rates—Fig. 11a versus Fig. 11b—were likely caused by the anelastic or inelastic deformation that combined with the linear elastic deformation to form the initial linear segment of the stress–strain curve.

In summary, the static elastic modulus was evaluated for the In–Pb–Ag solder counterpart to the Pb-free, In–Ag alloy. The modulus values were generally higher than those of the In–Ag solder, particularly at the lower temperatures. Unlike the In–Ag solder, the In–Pb–Ag alloy exhibited a step-wise decrease of the modulus values as a function of test temperature between 25°C and 75°C for the slower strain rate. At the faster strain rate, the stepped decrease of static elastic modulus occurred at 75°C. With only a single exception, this behavior was independent of annealing condition.

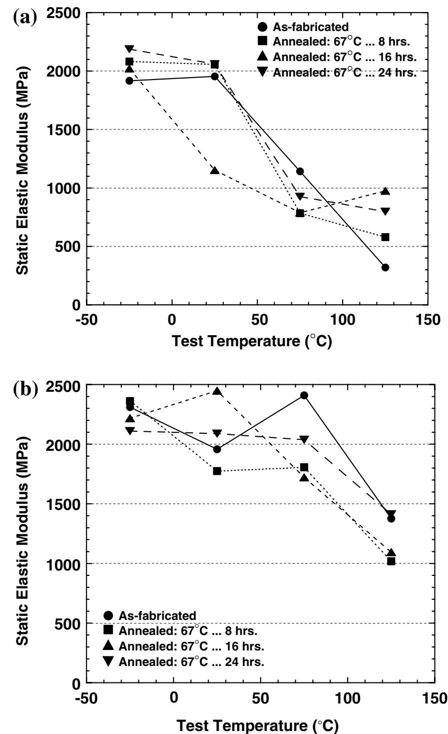

Fig. 11 Static elastic modulus (mean) as a function of test temperature for the In–Pb–Ag solder. The samples were in the as-fabricated condition as well as after having been annealed at 67°C for 8, 16, and 24 h. The two plots showed the moduli for the two strain rates (**a**) 4.4×10^{-5} s^{-1} and (**b**) 8.8×10^{-4} s^{-1}

3.2 In–Sn and In–Sn–Pb–Cd solders—compression stress–strain data

The yield stress and static elastic modulus properties were examined for the Pb-free, lower melting temperature In–Sn solder and the counterpart Pb-(and Cd-) containing In–Sn–Pb–Cd alloy. Shown in Fig. 12a, b are true-stress, true-strain curves representing the case of as-fabricated samples tested at –25°C for the strain

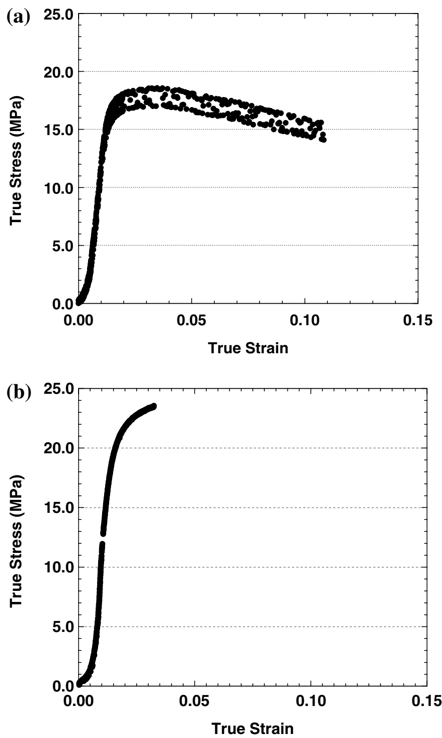

Fig. 12 Stress–strain curve of the In–Sn solder, tested in the as-fabricated condition at –25°C and strain rates of (**a**) 4.4×10^{-5} s^{-1} and (**b**) 8.8×10^{-4} s^{-1}

rates 4.4×10^{-5} s^{-1} and 8.8×10^{-4} s^{-1}, respectively. Three phenomenon were apparent in Fig. 12a. First, there was the slow ramp-up in the stress with increased strain. Sample misalignment was ruled out. Secondly, the plot in Fig. 12a showed fluctuations in the stress value as a function of deformation. Those fluctuations were not caused by jitter in the test frame nor by chatter in the electrical signal. Rather, this behavior was caused by a ratcheting effect of the deformation within the microstructure of the solder. Third, post-yield stress deformation exhibited a substantial strain softening effect. The strain-softening effect was noted in the shear stress–strain tests reported by Goldstein and Morris [3]. There were no indications that crack development was responsible for the decreasing stress. These three phenomena were also observed in samples exposed to one of the three annealing conditions prior to testing at –25°C. There were no consistent trends to suggest that these behaviors had a significant dependence on the annealing time at 52°C.

The stress–strain curve in Fig. 12b showed the effect of the faster strain rate of 8.8×10^{-4} s^{-1} on the deformation of the as-fabricated, In–Sn solder at –25°C. The ratcheting effect was eliminated from the curve, albeit, this particular plot did not show the deformation after yield stress. The extent of the initial stress ramp-up behavior was slightly reduced at the faster strain rate and it exhibited no observable dependence on the annealing treatment. Also, as was the case at the slower strain rate, the stress ramp-up effect was unique to the tests performed at –25°C. Tests that were continued past the yield stress exhibited strain softening.

The ratcheting and slow stress ramp-up phenomena were considered with respect to microstructural mechanisms. The ratcheting behavior has typically been associated with the start-stop movement of dislocations. The ‘‘stop’’ segment would also be a source of work hardening in the material. At the relatively high homologous temperatures at which these tests were performed, thermal activation should allow dislocations to jump past barriers, thereby lessening the likelihood for a ratcheting phenomenon. Moreover, dynamic recovery/recrystallization process would become apparent through strain-softening effects. This discrimination between low and high homologous temperature behaviors did not apply to the In–Sn solder at –25°C since *both* phenomena—ratcheting and strain softening—were observed in the samples.

The second phenomenon, the slow stress ramp-up at the beginning of deformation, suggests that there was a significant number of low-activation energy ‘‘defect sites’’ that were associated only with anelastic or inelastic deformation at –25°C. As the strain increased, those sites were used up so that the higher activation energy sites then contributed to the anelastic or inelastic deformation prior to yielding, increasing the slope of the plot. (Of course, the anelastic or inelastic deformation was occurring simultaneously with the linear elastic deformation.) At the faster strain rate (and higher test temperatures where the phenomenon was not observed), these low-activation sites would be rapidly used up, resulting in a loss of the slow, stress ramp-up effect. This mechanism would not be applicable to linear elastic deformation, since the latter does not occur by thermal activation, per se. Therefore, the stress ramp-up phenomenon provided further evidence that an anelastic or inelastic deformation mode contributed to the initial, linear deformation of the material before yielding took place.

The stress–strain curves were also investigated for the higher test temperatures. In all of those cases, the annealing treatments had very little impact on the

deformation performance. Also, the stress ramp-up behavior, which was observed at –25°C, did not reappear at the higher test temperatures. Shown in Fig. 13 are the stress strain curves obtained from as-fabricated specimens that were tested at (a) $4.4 \times 10^{-5}\ s^{-1}$ and (b) $8.8 \times 10^{-4}\ s^{-1}$. Significant strain softening was observed after the yield stress in both cases. In fact, the extent of strain softening appeared to be greater at the faster strain rate, indicating that dynamic recovery/recrystallization was overwhelming work hardening in the solder. Similar behaviors were observed at 75 and 100°C; the latter case being represented by the stress–strain curves in Fig. 14. The extent of strain softening was greater at the faster strain rate. As noted above, the annealing treatments did not significantly change the stress–strain behavior of the In–Sn solder.

The stress–strain curves in Figs. 12–14 and associated discussion indicated that the In–Sn solder experienced significant strain softening during stress–strain testing. Strain softening can be taken into account in the development of a constitutive model representing the deformation map of this material. From the applications point-of-view, strain softening provides a mechanism to relieve residual stresses effectively in the solder joint in the event that the solder surpasses its yield stress in a particular application. It is not conclusive that, because of strain softening, the In–Sn solder will have an inherently shorter cyclic lifetime. Such a conclusion must await a more extensive program of fatigue testing for this material.

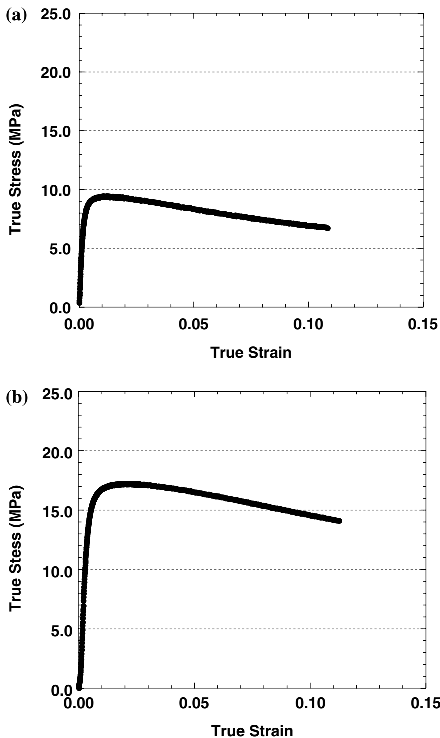

Fig. 13 Stress–strain curve of the In–Sn solder, tested in the as-fabricated condition at 25°C and strain rates of (**a**) $4.4 \times 10^{-5}\ s^{-1}$ and (**b**) $8.8 \times 10^{-4}\ s^{-1}$

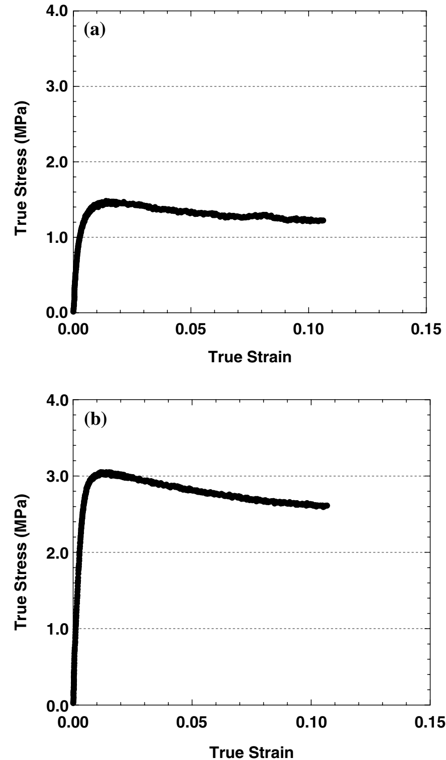

Fig. 14 Stress–strain curve of the In–Sn solder, tested in the as-fabricated condition at 100°C and strain rates of (**a**) $4.4 \times 10^{-5}\ s^{-1}$ and (**b**) $8.8 \times 10^{-4}\ s^{-1}$

The yield stress behavior was documented for the In–Sn solder. The data scatter was very similar to that observed for the In–Ag solder in Fig. 4 and, thus, will not be discussed further here. The mean yield stress as a function of test temperature was plotted in Fig. 15. Both strain rates and all annealing times (52°C) were represented in the graph. As expected, the yield stress decreased with increased test temperature. Also, the slower strain rate resulted in lower yield stresses than

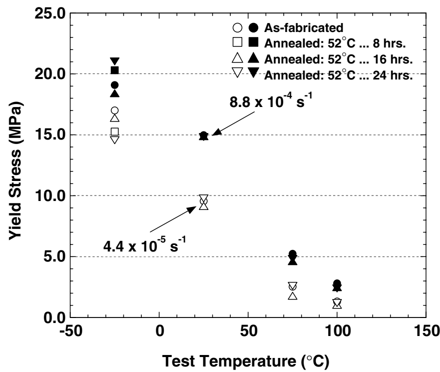

Fig. 15 Yield stress as a function of test temperature and annealing times (52°C) for the In–Sn solder. The open and closed symbols indicated the 4.4×10^{-5} s^{-1} and the 8.8×10^{-4} s^{-1} strain rates, respectively

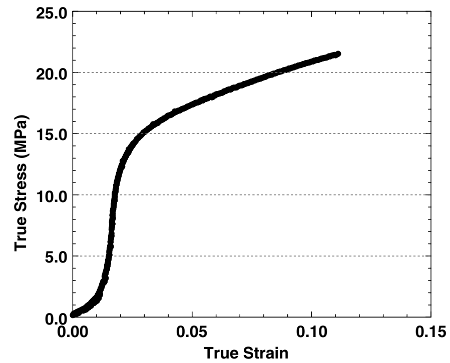

Fig. 16 Stress–strain curve of an as-fabricated In–Sn–Pb–Cd solder specimen tested at –25°C and at a strain rate of 8.8×10^{-4} s^{-1}

the faster strain rate; that difference diminished with increasing test temperature. The annealing time appeared to have a significant effect on the yield stress only for tests performed at –25°C. And, even in that sole case, there was no consistent trend between annealing time and yield stress value. In summary, the yield stress of the In–Sn solder, like the stress–strain deformation overall, was insensitive to the starting microstructure of the solder as established by the annealing conditions. The one possible exception, albeit quite weak, was observed for tests performed at –25°C.

A comparison was made between the yield stress values of the In–Sn solder (Fig. 15) and those of the higher melting temperature, Pb-free In–Ag solder (Fig. 5). At test temperatures of 75 and 100°C (In–Sn) or 125°C (In–Ag), the two alloys exhibited very similar yield stresses. However, in stress–strain tests at 25 and –25°C, the In–Sn solder, in spite of its lower melting temperature, had a higher yield strength than did the In–Ag solder at both strain rates. This comparison showed that the melting temperature was a poor indicator of the stress–strain behavior.

The stress–strain curves were examined for the In–Sn–Pb–Cd alloy. Although the topic of this paper is Pb-free solders, it was interesting to note the stress–strain curves from this particular alloy versus test temperature, strain rate, and annealing time. Shown in Fig. 16 is the stress–strain curve of the as-fabricated sample tested at the fast strain rate of 8.8×10^{-4} s^{-1} and test temperature of –25°C. The plot began with a stress ramp-up as was similarly observed for the In–Sn solder tested under these conditions. After the yield stress, the material exhibited work hardening, which was contrary to the strain softening experienced by the In–Sn solder. A plot that was nearly identical to that in Fig. 16, was observed for the In–Sn–Pb–Cd solder when tested at the slower strain rate, except for a slightly reduced rate of work hardening. At both strain rates, the annealing treatment did not significantly affect the stress–strain response.

The stress–strain behavior of the In–Sn–Pb–Cd solder changed when the test temperature was raised to 25°C. At both strain rates, the slow stress ramp-up prior to linear deformation was lost. This observation was illustrated in Fig. 17, which shows the stress–strain curve of the as-fabricated sample tested at 4.4×10^{-5} s^{-1}. It was also noted in Fig. 17 that the post-yield stress deformation began with a slight degree of strain softening followed with a small amount of work hardening. At the faster strain rate, the entire plastic deformation

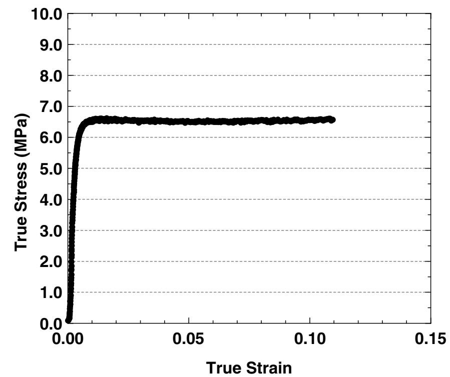

Fig. 17 Stress–strain curve of the as-fabricated In–Sn–Pb–Cd solder tested at 25°C and a strain rate of 4.4×10^{-5} s^{-1}

regime exhibited work hardening, albeit, to a lesser degree than was observed in Fig. 16. At both strain rates, the annealing times did not significantly affect the stress–strain behavior of the In–Sn–Pb–Cd solder.

The stress–strain tests performed at 75°C resulted in entirely different deformation behaviors. At the 4.4×10^{-5} s^{-1} rate, the as-fabricated specimens exhibited fluctuations in the stress values as shown in Fig. 18a. The peak-to-peak difference was 0.1 MPa and the strain period was approximately 0.02. The magnitude of the fluctuations diminished with increased annealing time, resulting in a stress–strain curve very similar to that in Fig. 17. The stress–strain curve of the as-fabricated sample tested at the faster strain rate of 8.8×10^{-4} s^{-1} was shown in Fig. 18b. A peak in the stress was followed by strain softening, which in turn, was followed by a strain hardening behavior. The annealing treatment had no noticeable effect on the stress–strain plot at the faster strain rate; all curves were similar to Fig. 18b.

Lastly, the stress–strain curves were investigated for the In–Sn–Pb–Cd solder exposed to tests at 100°C. Plots representing the two strain rates and the as-fabricated condition were provided in Fig. 19. Both curves had generally the same shape except that the sequence of a stress maximum and strain softening followed by work hardening was clearly more distinct at the faster strain rate (Fig. 19b). Very slight fluctuations appeared in the curves generated by the annealed samples tested at 4.4×10^{-5} s^{-1}. At the faster strain rate, the annealing treatments caused a decrease in the stress maximum after yielding. These were the only effects manifested by the annealing treatments on the In–Sn–Pb–Cd stress–strain behavior.

In summary, the stress–strain behavior was examined for the In–Sn–Pb–Cd solder. A particular emphasis was placed on this Pb-and Cd-bearing alloy to illustrate the different deformation behaviors that can occur with these more complex, low-temperature metal alloys. It was fortuitous that such variable

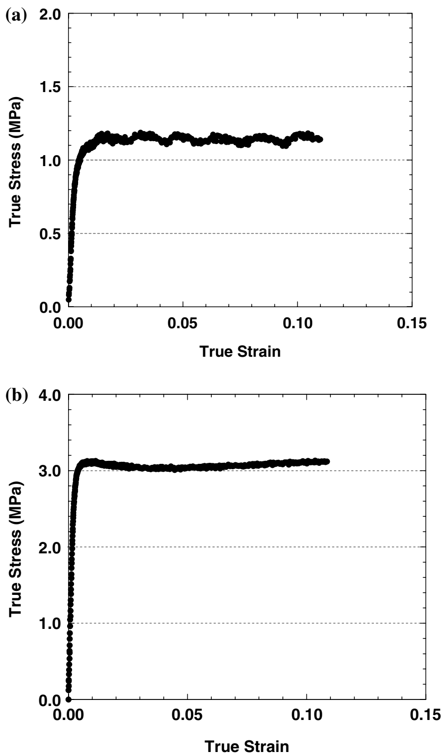

Fig. 18 Stress–strain curve of the In–Sn–Pb–Cd solder, tested in the as-fabricated condition at 75°C and strain rates of (**a**) 4.4×10^{-5} s^{-1} and (**b**) 8.8×10^{-4} s^{-1}

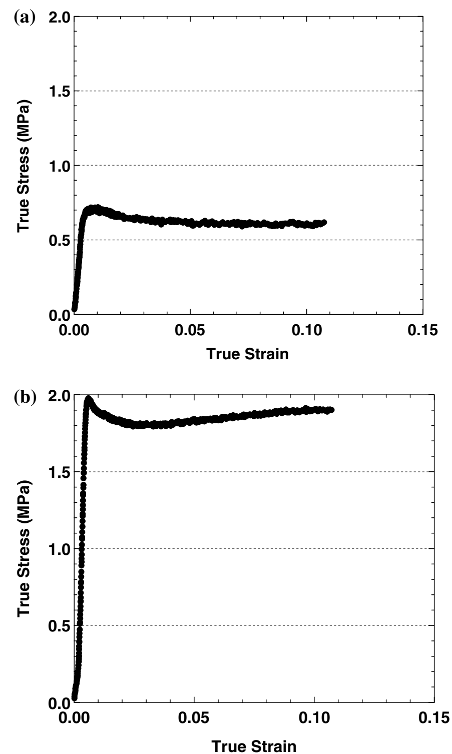

Fig. 19 Stress–strain curve of the In–Sn–Pb–Cd solder, tested in the as-fabricated condition at 100°C and strain rates of (**a**) 4.4×10^{-5} s^{-1} and (**b**) 8.8×10^{-4} s^{-1}

behavior happened to a lesser degree with the Pb-free, In–Sn solder, implying that the latter alloy had a more stable microstructure. That stability will provide for a more predictable response to an applied stress, which facilitates the development of a higher fidelity computational model. For either solder, it was interesting to note that the annealing treatments had, in general, very little effect on the stress–strain curve. This observation showed that the individual solder microstructures that were generated by the casting process, were relatively stable.

The yield stress values as a function of test temperature and annealing treatment were compiled for the In–Sn–Pb–Cd solder in Fig. 20. The trends were unique vis-à-vis the other solders discussed, thus far. The yield stresses were nearly identical at –25°C for *both* strain rates and *all* annealing times (at 52°C). Then, the yield stresses were more distinguished by strain rate with increasing test temperatures. However, that difference was greatest at 25°C; it then diminished with the 75 and 100°C test temperatures. Also, at the test temperatures of 25, 75, and 100°C, the yield stress remained insensitive to annealing time.

The yield stress data for the In–Sn–Pb–Cd solder were compared to the In–Sn solder (Fig. 15). The aforementioned strain rate sensitivity of the In–Sn–Pb–Cd solder, particularly at –25°C, was contrary to the behavior of the In–Sn solder. The values of the In–Sn–Pb–Cd solder were less than those of the In–Sn solder, more so at the two lowest test temperatures of –25 and 25°C. On the other hand, both solders were similar with respect to the absence of a sensitivity to annealing treatment at test temperatures of 25, 75, and 100°C.

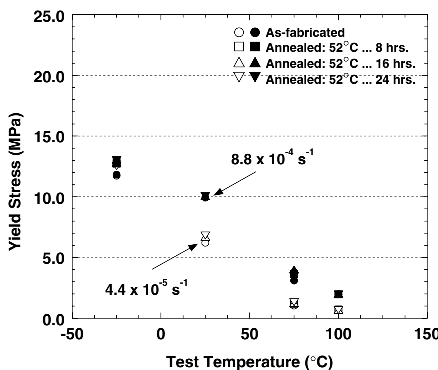

Fig. 20 Yield stress as a function of test temperature and annealing time (52°C) for the In–Sn–Pb–Cd solder. The open and closed symbols indicated the 4.4×10^{-5} s^{-1} and the 8.8×10^{-4} s^{-1} strain rates, respectively

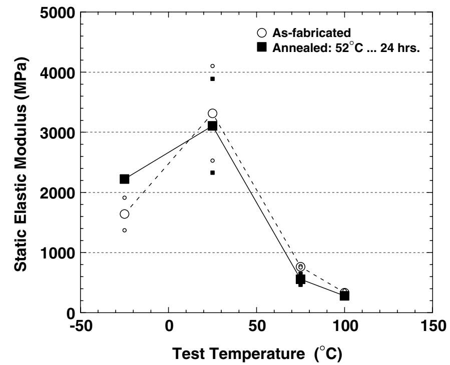

Fig. 21 Static elastic modulus as a function of test temperature for the In–Sn solder. The strain rate was 4.4×10^{-5} s^{-1}. The two sample conditions, as-fabricated and annealed at 24 h (52°C) were represented. The large symbols are the mean values; the smaller symbols are the two individual maximum and minimum points

The static elastic modulus was also investigated for the In–Sn and In–Sn–Pb–Cd solders. Shown in Fig. 21 are the modulus values as a function of test temperature for the In–Sn solder, representing the as-fabricated and the 24 h annealing time (52°C). Figure 21 exemplified the scatter observed for the individual values. The variability was greatest at 25°C; it was slightly less at –25°C and became negligible at 75 and 100°C. The scatter was largely independent of the sample annealing conditions. At the faster strain rate, the maximum variability was observed at –25°C. The scatter decreased with increasing temperature. Lastly, differences of static elastic modulus between the two strain rates decreased with higher test temperature. Although difficult to explain from a microstructural standpoint, it is clear that these trends reflect the contribution of the anelastic or inelastic deformation process. A more consistent behavior would have been reflected in this data if only linear elastic deformation were the controlling phenomenon. This point is further evidenced in the following discussion.

The In–Sn static elastic modulus was plotted as a function of test temperature in Fig. 22a and b for the 4.4×10^{-5} s^{-1} and 8.8×10^{-4} s^{-1} strain rates, respectively. All of the annealing conditions were represented in the graph. In Fig. 22a, the modulus appeared to be sensitive to the annealing time only at –25 and 25°C, but not in a consistent manner. All values were nearly the same at the two highest test temperatures. Overall, the modulus values did not change monotonically with test temperature. In fact, the plot indicated two regimes; the high modulus values for –25 and 25°C

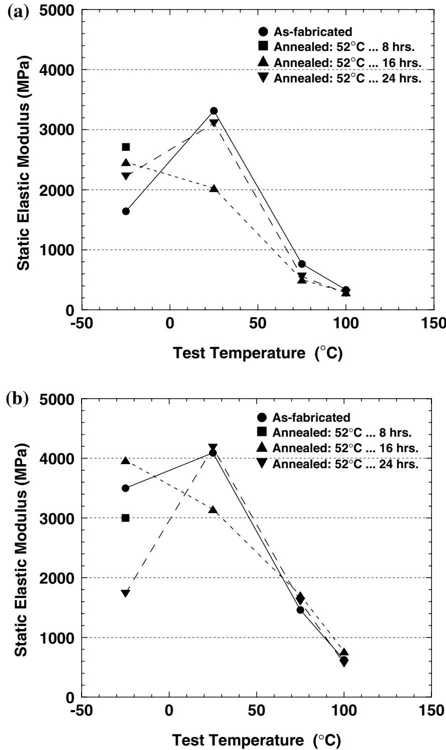

Fig. 22 Static elastic modulus (mean) as a function of test temperature and annealing condition for the In–Sn solder. The two plots showed the modulus for the two strain rates (**a**) 4.4×10^{-5} s^{-1} and (**b**) 8.8×10^{-4} s^{-1}

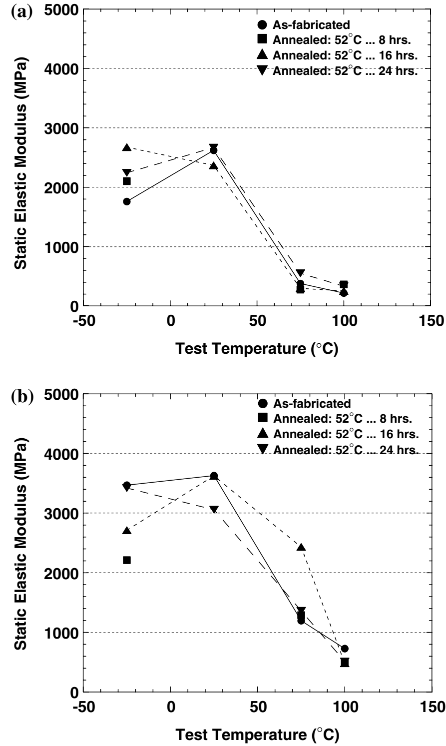

Fig. 23 Static elastic modulus (mean) as a function of test temperature and annealing condition for the In–Sn–Pb–Cd solder. The two plots showed the modulus values for the two strain rates; (**a**) 4.4×10^{-5} s^{-1} and (**b**) 8.8×10^{-4} s^{-1}

and low modulus values for 75 and 100°C. The same trends were observed at the faster strain rate (Fig. 22b). In the latter case, the modulus values were slightly higher at each of the test temperatures.

The static elastic modulus values were also examined for the In–Sn–Pb–Cd solder. The scatter ranges were similar to those observed for the In–Sn solder except for less spread at 25°C. Shown in Figs. 23a and b are the modulus values of the In–Sn–Pb–Cd solder for the two strain rates. The trends and magnitudes observed in Fig. 23a and b were nearly identical to those observed for the In–Sn solder in the corresponding Fig. 22a and b, respectively.

In summary, the yield stress and static elastic modulus values were compiled for the In–Sn and In–Sn–Pb–Cd solders. Both solders exhibited a decreasing yield stress with increased temperature and slower strain rate. The In–Sn solder had higher yield stress values than the In–Sn–Pb–Cd solder, particularly at the two lowest temperatures. In both cases, the annealing treatment did not have either a significant or consistent effect on the yield stress. The static elastic modulus values were lower by an order of magnitude than expected, due to the anelastic or inelastic deformation mode that was hypothesized to have accompanied linear elastic deformation. The modulus dependence on test temperature exhibited two regimes, a low-temperature regime of higher values at –25 and 25°C and a high-temperature regime of lower values at 75 and 100°C. The step-wise temperature dependence was more distinct at the slower strain rate. To within experimental error, the modulus values were similar between the two solders.

It was possible to hypothesize some approximate effects of the solder deformation properties on interconnection reliability and the development of computational models for the In–Sn and In–Sn–Pb–Cd solders. (The effects are only approximate in the sense that creep deformation, which is discussed below, has an important role, as well.) The static modulus values

were generally comparable between the two solders at each temperature so that both alloys have similar capacities to relieve residual stresses by linear anelastic/elastic deformation. Assuming that the stress levels are sufficiently high so that inelastic deformation occurs in the solders, the higher yield stress of the In–Sn alloy would cause it to be less capable of relieving those stresses than the Pb- and Cd-bearing counterpart alloy, particularly at the lower temperatures.

Finally, it was observed that the yield stresses and static elastic moduli were relatively insensitive to the annealing treatments. This trend will improve reliability predictions because the material properties are less likely to depend upon the processing parameters used to make electrical interconnections.

3.3 In–Ag and In–Pb–Ag solders—compression creep data

Compression creep tests were performed on the Pb-free, In–Ag solder and its Pb-bearing counterpart, the In–Pb–Ag alloy. The strain-time curves of the In–Ag solder have been summarized in Fig. 24a–d. Only the creep curves representing the as-fabricated condition were presented because the generalized strain-time behavior was similar for those samples exposed to the 67°C, 16 h annealing treatment before creep testing. In a number of cases, in particular, the reduced stresses at the lowest temperatures, the positive creep strain was negligible. Therefore, the associated strain-time curves were simply omitted from the composite plots described below vis-à-vis the targeted stresses listed in Table 2.

The purpose of discussing the curves in Fig. 24 was to appreciate the long-term deformation behavior of these solders. Recall that creep will comprise a large part of the deformation that occurs during the service life (and accelerated aging) of the solder joints. In addition, the characteristics of the strain–time curves, and the stability of those curves with respect to the starting microstructure (annealing treatment), determine the complexity that is required of the UCP

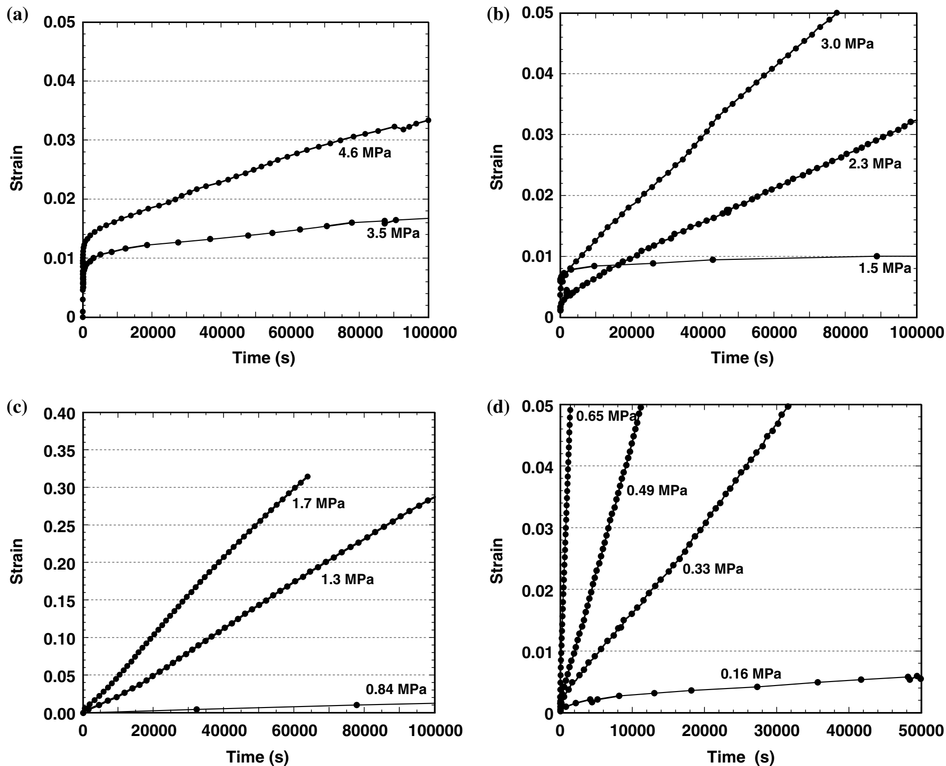

Fig. 24 Creep curves of the In–Ag solder tested in the as-fabricated, representing the following temperature conditions: (**a**) –25°C; (**b**) 25°C; and (**c**) 75°C, and (**d**) 125°C

constitutive model to accurately predict the creep component (''C'' in UCP) of the overall deformation behavior.

It should be recalled that the applied stresses were not selected arbitrarily. Rather, the stress values were selected, based upon approximately 20%, 40%, 60%, and 80% of the yield stress. Therefore, when the material yield stress is used as an upper-limit design criterion for mechanical strength, an interconnection would be expected to experience stresses at levels that are commensurate with those percentages in engineering applications.

The In–Ag creep curves representing the temperatures of –25 and 25°C were shown in Fig. 24a and b. The strain–time plots showed both primary and secondary or steady-state creep stages. The primary creep stage became a lesser proportion of the curves when the test temperature was raised from –25 to 25°C. The creep curves representing tests performed at 75 and 125°C were shown in Fig. 24c and d and indicated that the deformation was largely steady-state creep. There was very little contribution by primary creep except for the 0.16 MPa test performed at 125°C. At 75°C (Fig. 24c), the creep curves had a sigmoidal shape. Sigmoidal creep indicates that there was initially an insufficient quantity of defects present in the material to support deformation, resulting in a delayed start of deformation [7]. Therefore, it was necessary to first generate the defects that could then respond to the applied stress, resulting in the subsequent increase in the strain rate.

Lastly, the creep curves in Fig. 24 did not show an obvious tertiary stage. Tertiary creep, which is indicated by an accelerating strain rate with time, occurs when large-scale damage, i.e. cracks, have been generated in the microstructure. Although the current methodology is based on compression testing, critically resolved shear stresses (CRSSs) can prevail in the specimen microstructure that are capable of creating damage that culminates into crack development. Similarly, diffusion-based mechanisms, primarily based on the movement of vacancies, can form discontinuities that develop into cracks, irrespective of the ''sign'' of the applied stress. Therefore, the absence of a tertiary creep stage in the deformation curves in Fig. 24 indicated that large-scale damage was not generated in the samples.

The minimum strain rate observed during steady-state creep, $d\varepsilon/dt_{min}$ (s^{-1}) was evaluated as a function of temperature, T (K), and stress, σ (MPa), per equation (3). The resulting expressions for the as-fabricated and post-annealed conditions are shown as Eqs. 4 and 5 below:

$$d\varepsilon/dt_{min} = 2.8 \times 10^{8} \sinh^{3.2 \pm 0.5}(1.075\sigma) \exp(-99 \pm 14/RT) \quad (4)$$

$$d\varepsilon/dt_{min} = 2.8 \sinh^{1.1 \pm 0.4}(1.500\sigma) \exp(-46 \pm 11/RT) \quad (5)$$

The R^2 values for Eqs. 1 and 2 were 0.90 and 0.69, respectively. The error terms represented the 95% confidence interval. The reduced R^2 value for the annealed samples was somewhat unexpected. It was anticipated that the annealing treatment would stabilize the solder microstructure to produce a more consistent creep behavior. It is evident that the aging treatment had the opposite effect in this regard. All parameters except for the stress coefficient, α, were reduced by the aging treatment; the opposite trend was observed in the case of α.

Some insight was sought into the possible physical mechanisms active during creep from the sinh law parameters. The sinh law exponent (p) values were commensurate with those observed for the Sn–Pb eutectic solder [14]. Unfortunately, only relative comparisons can be drawn between the values of p since the latter has not been correlated to particular creep mechanisms or microstructural features. A similar situation prevailed with respect to f_0 and α.

On the other hand, the apparent activation energy, ΔH, can provide some insight into the rate-controlling mechanism of creep. It has been observed by other investigators that, when lattice or bulk diffusion is the controlling mechanism, ΔH will have values that are typically 90–110 kJ/mol for metals and alloys [17, 18]. When the controlling mechanism is fast or short-circuit diffusion, such as the movement of vacancies or interstitials along grain and/or interface boundaries, the value of ΔH is typically 0.4–0.6 of the bulk diffusion value, or about 40–60 kJ/mol [19–21]. According to these benchmarks, lattice diffusion controlled creep of the as-fabricated In–Ag samples. On the other hand, the annealing treatment caused the creep rate-controlling mechanism to shift to short-circuit diffusion. Two microstructural changes could have likely resulted from the annealing treatment. (1) The annealing treatment eliminated point and line defects such as vacancies and dislocations, respectively, through recovery. Because these defects supported lattice diffusion, the creep deformation had to be carried by grain and phase boundary processes. (2) The second hypothesis was that the annealing treatment simply increased the number of grain and phase boundaries through the early stages of recrystallization in which newly created grains have not yet begun to consume the older grains.

The poor correlation accompanying Eq. 5 can often be traced to a temperature dependence of the rate kinetics. In order to test this hypothesis, the data set was divided into two regimes, a low-temperature regime comprised of the –25 and 25°C results and the high-temperature regime that included the 75 and 125°C data. The resulting kinetics equations were described by Eqs. 6a, b, respectively:

$$[-25, 25\,^{\circ}\mathrm{C}] \quad \mathrm{d}\varepsilon/\mathrm{d}t_{\min} = 0.19\sinh^{0.9\pm0.3}(1.500\sigma)\exp(-37\pm12/RT) \tag{6a}$$

$$[75, 125\,^{\circ}\mathrm{C}] \quad \mathrm{d}\varepsilon/\mathrm{d}t_{\min} = 3.6\times10^{9}\sinh^{1.8\pm0.6}(1.500\sigma)\exp(-113\pm23/RT) \tag{6b}$$

For simplicity, the α value was allowed to remain unchanged, since the prior analyses used to obtain Eq. 5 showed a minimal degree of sensitivity to it. The higher R^2 values were 0.81 and 0.83, respectively, indicating that the steady-state creep rate kinetics were dependent on temperature. The data were also evaluated by grouping the 25°C results together with the 75 and 125°C data. A low R^2 value of 0.55 was obtained, indicating that the 25°C data was better grouped with the –25°C results and that the mechanism change occurred between 25°C and 75°C.

A comparison of Eqs. 6a and b indicated that the sinh term exponent increased from the low-temperature to the high temperature regime; however, the difference was not statistically significantly. On the other hand, the high-temperature regime exhibited a higher apparent activation energy value, indicating that bulk diffusion controlled the creep deformation. Fast-diffusion remained the rate-controlling mechanism for creep in the low-temperature regime. Similar trends of ΔH have been observed in the creep behavior of other engineering alloys [10].

The effect of the annealing treatment on steady-state creep was illustrated by the plot in Fig. 25 that shows the minimum strain rate calculated by Eqs. 4 and 5 over a 0–4 MPa stress range and concurrent test temperatures. The annealing treatment caused the strain rate to become less sensitive to temperature because the curves were closer together in the vertical direction. The strain rate was also less sensitive to the applied stress after the annealing treatment as indicated by the reduced slope of the curves. Beyond these summarizations, the fact that, for the same test temperature, the curves corresponding to the as-fabricated and annealed conditions crossed one-another indicated that no hard-and-fast rules could be formulated for predicting, in general, the effect of annealing treatment on the steady-state creep rate.

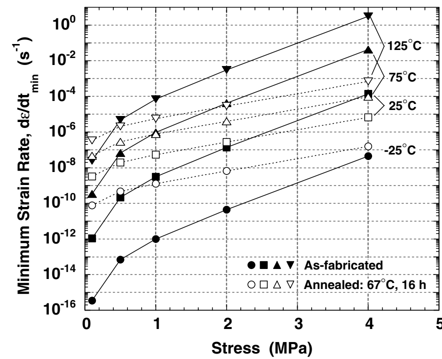

Fig. 25 Plot of the sinh law equations of steady-state creep strain rate for the In–Ag solder in the as-fabricated condition and after annealing at 67°C for 16 h

The strain-time creep curves are shown in Fig. 26 for the In–Pb–Ag solder in the as-fabricated condition. As was the case with the In–Ag solder, there was very little primary creep exhibited for the applied stresses and temperatures. Steady-state creep dominated the deformation from the onset of testing for all, but the –25°C experiments in which a slightly greater proportion of primary creep was observed. Also, the creep curves did not exhibit a tertiary stage that was indicative of large-scale damage.

The creep behavior of the In–Pb–Ag solder was compared to that of the In–Ag solder by examining Figs. 24 and 26, respectively. The In–Ag solder experienced a greater degree of creep strain for the stress range of approximately 3–8 MPa and comparable test temperatures. The greater creep strain implied that the In–Ag solder could more readily relieve residual stresses in engineering structures than could its Pb-bearing counterpart.

The strain rate kinetics of the In–Pb–Ag solder were represented by the sinh law expression shown in Eq. 7 for the as-fabricated condition:

$$\mathrm{d}\varepsilon/\mathrm{d}t_{\min} = 3.3\times10^{9}\sinh^{2.9\pm0.3}(0.050\sigma)\exp(-74\pm5/RT) \tag{7}$$

The R^2 value of the regression analysis was 0.97 showing a very good correlation. For the sake of brevity, this analysis was not discussed for the In–Pb–Ag solder following the annealing treatment. A comparison was made between Eq. 7 and 4, the latter representing the In–Ag solder in the as-fabricated condition. The sinh term exponents were similar;

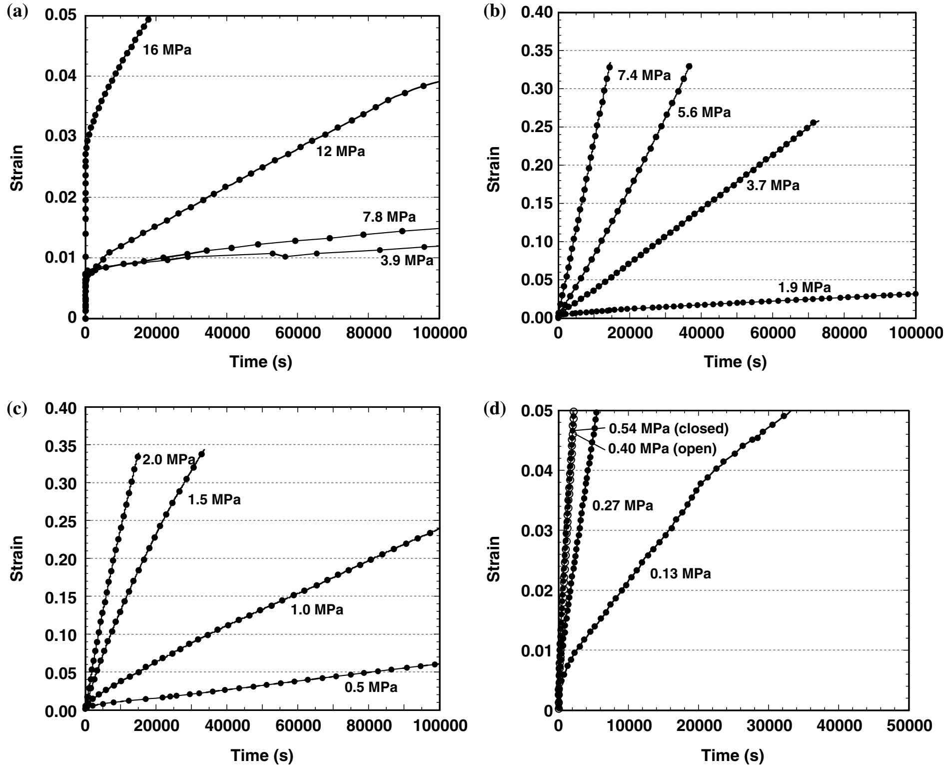

Fig. 26 Creep curves of the In–Pb–Ag solder tested in the as-fabricated, representing the following temperature conditions: (**a**) –25°C; (**b**) 25°C; and (**c**) 75°C, and (**d**) 125°C

however, the lower apparent activation energy of Eq. 6 indicated that short-circuit or fast-diffusion mechanisms governed In–Pb–Ag creep in the as-fabricated condition. Also, the stress coefficient, α , equal to 0.05 for the In–Pb–Ag alloy was nearly two orders of magnitude less than 1.075 for the In–Ag solder.

A direct comparison was made of the sinh law strain rate Eqs. 4 and 7 representing the In–Ag and In–Pb–Ag solders, respectively, in the as-fabricated condition. The corresponding plot is shown in Fig. 27. Because the curves were closer together, the steady-state strain rate of the In–Pb–Ag solder was less sensitive to test temperature than was the In–Ag solder. Similarly, the steady-state strain rate was less sensitive to stress as was evidenced by the reduced slope at stresses greater than 0.5 MPa. Overall, a comparison of creep behaviors between the two solders depends upon temperature and applied stress. At stresses below 2 MPa, the In–Ag solder exhibited a lower strain rate than the In–Pb–Ag alloy. The relative ranking went through a transition in the stress range of 2–4 MPa so that, at stresses greater than 4 MPa, the In–Ag solder clearly had a faster strain rate than its Pb-bearing counterpart.

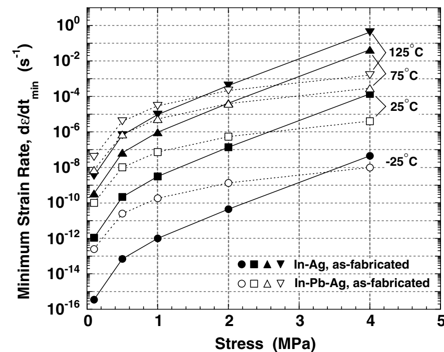

Fig. 27 Plot of the sinh law equations of steady-state creep strain rate comparing the In–Ag and In–Pb–Ag solders in the as-fabricated condition

Therefore, in terms of steady-state creep, which appeared to predominate the creep curves of these two alloys, the relative effectiveness of reducing residual stresses in complex OE devices through creep deformation will be a function of the residual stress level and the temperature conditions.

In summary, the creep behavior was investigated for the In–Ag and counterpart In–Pb–Ag solders. The strain time curves of the In–Ag solder showed largely the steady-state stage. Only a limited degree of primary creep was observed and the tertiary stage was absent from the curves of both alloys. Similar strain-time trends were also observed in the samples following the annealing treatment. In the case of the In–Ag solder, the decrease of ΔH after the annealing treatment changed the creep mechanism from bulk diffusion to a short-circuit diffusion mechanism. The creep curves of the In–Pb–Ag solder exhibited the same qualitative trends. It was clear that the degree of creep strain exhibited by the In–Ag solder with respect to the In–Pb–Ag solder depended upon the applied stress and temperature conditions. It was safe to conclude that, above 4 MPa, the In–Ag solder exhibited a greater propensity for creep deformation than did its Pb-free counterpart.

3.4 In–Sn and In–Sn–Pb–Cd solders—compression creep data

The creep behaviors were examined for the two lower melting temperature solders, In–Sn and In–Sn–Pb–Cd. The strain-time plots of the In–Sn solder were shown in Fig. 28. Creep deformation at –25°C (Fig. 28a) exhibited very little primary creep; the deformation was almost entirely steady-state creep. The plots representing the 10 and 13 MPa stresses showed a slight up-turn that suggested the beginning of tertiary creep. The appearance of tertiary creep, and whether it was caused by the accumulation of large-scale damage or was the result of more subtle changes within the In–Sn microstructure—e.g., defect density and/or defect velocity—will be explored below.

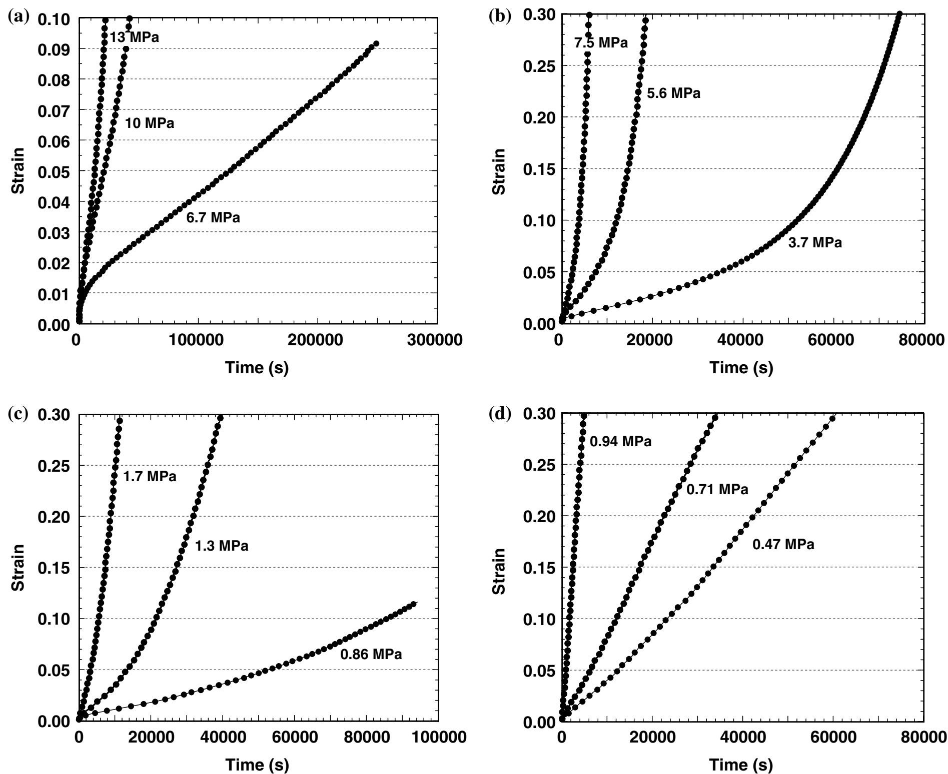

Fig. 28 Creep curves of the In–Sn solder tested in the as-fabricated, representing the following temperature conditions: (**a**) –25°C; (**b**) 25°C; and (**c**) 75°C, and (**d**) 100°C

The creep curves obtained from tests at 25°C were shown in Fig. 28b. Primary creep was nearly absent from the plots; rather, there was a short duration of steady-state creep followed by an extensive tertiary stage. The creep curves obtained at 75 and 100°C are shown in Fig. 28c and d, respectively. At 75°C, the shapes of the creep curves were very similar to those obtained at 25°C. There was an absence of significant primary stage, a short steady-state creep regime, and a significant tertiary creep stage. Unexpectedly, the tests performed at 100°C (Fig. 28d) showed a *reduced* extent of the tertiary stage. In fact, the tertiary behavior appeared to diminish with increased stress. Because primary creep was largely absent, these curves were primarily the steady-state stage.

An extensive microstructure analysis of the solders was not planned at the time of this study. However, the prevalence of the tertiary creep behavior in the In–Sn solder warranted an investigation of the In–Sn microstructure in order to determine whether large-scale damage was responsible for this tertiary behavior. Shown in Fig. 29 are low and high magnification optical micrographs of the as-fabricated In–Sn specimen that was creep tested at –25°C and 13 MPa. Individual cells, which are distinguished by different lamellae size and/or orientations, were separated by coarsened grain boundaries of both the In-rich β phase (dark) and Sn-rich γ phase (light). The coarsened boundaries were denoted by the white arrows in Fig. 29a. The micrograph in Fig. 29a, as well as the higher magnification image in Fig. 29b, clearly showed crack development along those coarsened cell boundaries. There was no evidence of phase boundary sliding or cracking within the cells, themselves. Similar coarsened boundary cracking was observed in the samples tested at 25 and 75°C, the latter case being shown in Fig. 30a. Therefore, at each of the three temperatures of –25, 25, and 75°C, microstructural damage in the form of cracking along coarsened, cell boundaries was responsible for the tertiary creep behavior observed in Fig. 28a–c.

Recall that, in Fig. 28d, which represented the creep tests performed at 100°C, tertiary stage was significantly reduced or absent altogether. Shown in Fig. 30b is an optical micrograph of the post-creep tested

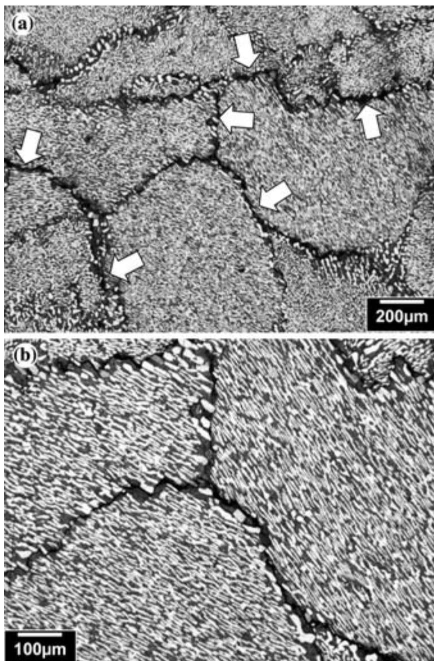

Fig. 29 Optical micrographs showing the In–Sn solder microstructure after creep testing at –25°C and 13 MPa, using two magnifications. The sample was tested in the as-fabricated condition

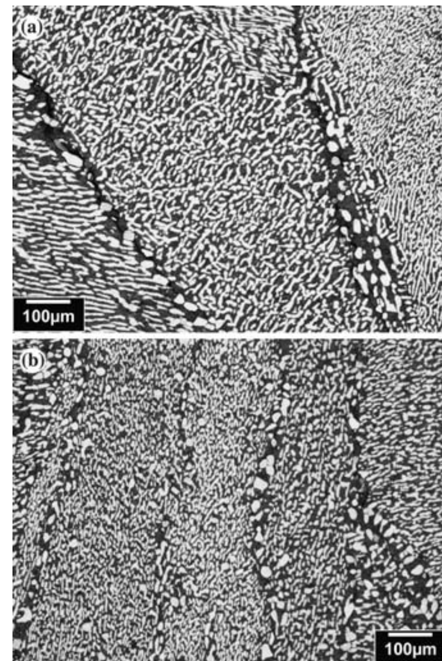

Fig. 30 Optical micrographs showing the In–Sn solder microstructure after creep testing under the following conditions: (**a**) 75°C, 1.7 MPa and (**b**) 100°C, 0.94 MPa. In both cases, the specimens were tested in the as-fabricated condition

sample exposed to a stress of 0.94 MPa at 100°C (see Fig. 28d). The coarsened boundaries were still present, although, they were less distinguishable from the generally more coarsened intracellular microstructure. Also, the extent of cracking in those coarsened boundaries was significantly reduced as compared to other temperatures. It was hypothesized that the coarser cell (interior) microstructure had taken up a greater share of the creep deformation, thereby relieving the boundaries of the need to generate cracks in response to the applied stresses.

The creep strain observed with the In–Sn solder (Fig. 28) was compared to that of the In–Ag solder (Fig. 24). The In–Sn solder exhibited a greater degree of creep strain at the equivalent test temperature and stress. This result was not surprising, given the In–Sn alloy's lower melting temperature.

The creep rate kinetics were also examined for the In–Sn solder. Equations 8 and 9 below express the minimum or steady-state creep rate as a function of applied stress and temperature for the as-fabricated and annealed (52°C, 16 h), respectively:

$$d\varepsilon/dt_{\min} = 5313 \sinh^{1.7\pm0.4}(0.325\sigma)\exp(-55 \pm 11/RT) \tag{8}$$

$$d\varepsilon/dt_{\min} = 687 \sinh^{1.5\pm0.6}(0.295\sigma)\exp(-48 \pm 13/RT) \tag{9}$$

The R^2 values were 0.83 and 0.73, respectively. It was interesting to note that the annealing treatment did not significantly change the sinh law exponent or the apparent activation energy. The value of α decreased only slightly following the annealing treatment; there was a greater decrease in the pre-exponential coefficient, f_0.

As was done in the case of the In–Ag solder, the low R^2 value of the annealed samples warranted further analysis to address the possibility that the apparent activation energy was dependent on temperature. The α value was kept the same. The results, which were very interesting, were presented by the three cases in Eq. 10a–c:

$$[-25, 25\ \mathrm{deg\,C}] \quad d\varepsilon/dt_{\min} = 27 \sinh^{1.5\pm0.6}(0.295\sigma)\exp(-41 \pm 13/RT) \tag{10a}$$

$$[75, 125\ \mathrm{deg\,C}] \quad d\varepsilon/dt_{\min} = 1.2 \times 10^{22} \sinh^{4.3\pm1.7}(0.295\sigma)\exp(-168 \pm 73/RT) \tag{10b}$$

$$[25\text{--}125\ \mathrm{deg\,C}] \quad d\varepsilon/dt_{\min} = 2.2 \times 10^{22} \sinh^{3.2\pm1.0}(0.295\sigma)\exp(-113 \pm 35/RT) \tag{10c}$$

The R^2 values were 0.81, 0.74, and 0.73, respectively. A higher correlation was obtained when the two lowest test temperature data sets (–25 and 25°C) were paired together. This was the same case for the In–Ag solder. The kinetics parameters were very similar between Eqs. 9 and 10a. On the other hand, very little improvement was observed in the R^2 value of the Eq. 10b when the two higher test temperatures were grouped together (75 and 100°C). By means of the apparent activation energy, Eq. 10a and b indicated that lattice diffusion controlled creep at the higher test temperatures and fast-diffusion controlled creep at the lower temperatures. However, from the viewpoint of developing a UCP constitutive model, Eq. 9 would provide a suitable representation of the creep behavior of the annealed In–Sn alloy.

The creep kinetics described above were compared to those obtained by Mei and Morris [2]. Although the latter authors tested the In–Sn solder in shear and described steady-state creep by a power law expression, it was expected that the kinetics would be similar. Recall that the cited tests were performed at 20, 65, and 90°C. The stress exponent and apparent activation energy values were 3.2 and 96 kJ/mol, respectively. These values were each considerably higher than those recorded in Eqs. 8 or 9. However, when compared to Eq. 10c for which, the –25°C data were eliminated, the kinetics parameters were similar to those in [2]. This comparison further substantiated the difference in creep mechanisms between the low and high-temperature regimes.

Equations 7 and 8 were plotted as a function of stress and temperature in Fig. 31. As expected, there was very little difference in the predicted strain rate between the as-fabricated and annealed conditions. These trends were in sharp contrast to the In–Ag solder for which, the annealing treatment caused a significant change in the steady-state creep kinetics.

The values of ΔH in Eqs. 7 and 8 were commensurate with grain or phase boundary (fast) diffusion during steady-state creep. The optical micrographs in Figs. 29 and 30 showed the extensive network of phase boundaries that prevailed in the two-phase microstructure of each cell. Those intra-cell diffusion processes culminated in the defects that accumulated at the cell boundaries, resulting in the formation of cracks that were the source of the pronounced tertiary creep in the In–Sn samples.

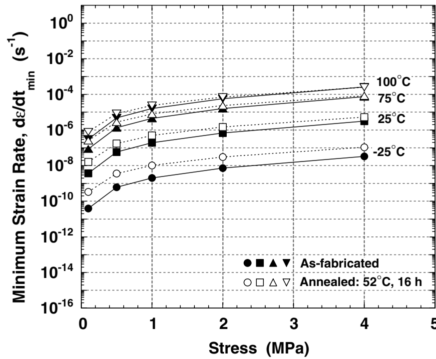

Fig. 31 Plot of the sinh law equations of steady-state creep strain rate for the In–Sn solder in the as-fabricated condition and after annealing at 52°C for 16 h

The strain-time curves for the In–Sn–Pb–Cd solder appear in Fig. 32 for each of the four test temperatures. At –25°C (Fig. 32a), there was significant primary creep preceding steady-state creep at each of the applied stresses. Although primary creep was also present in the creep curves generated at 25°C (Fig. 32b), the extent of primary creep diminished and the plots showed largely steady-state creep with increasing stress level. This same trend was observed at the test temperatures of 75°C (Fig. 32c) and 100°C (Fig. 32d). At all test temperatures and stresses, tertiary creep was not observed in the strain-time curves.

A comparison was made between the strain-time curves of the In–Sn solder (Fig. 28) and In–Sn–Pb–Cd alloy (Fig. 32) for comparable stresses and temperatures. At –25°C, the In–Sn solder shows slightly more creep strain than did the In–Sn–Pb–Cd alloy. However, at the three higher temperatures of 25, 75, and 100°C, the In–Sn solder exhibited noticeably less creep strain, in spite of the accelerated strain rate associated with the tertiary creep stage. The difference was particularly noticeable at 100°C where the tertiary stage was largely absent from the creep response of the In–Sn solder.

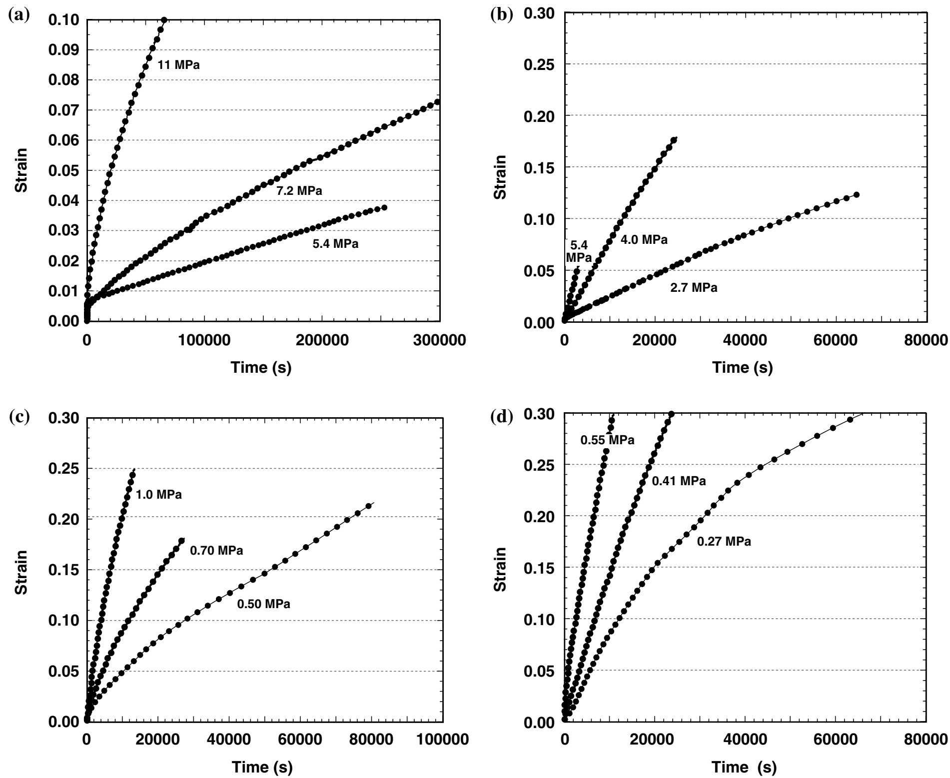

Fig. 32 Creep curves of the In–Sn–Pb–Cd solder tested in the as-fabricated, representing the following temperature conditions: (**a**) –25°C; (**b**) 25°C; and (**c**) 75°C, and (**d**) 100°C

Therefore, with the exception of tests performed at –25°C, the In–Sn solder appeared to be more creep resistant than its Pb-bearing counterpart.

The secondary creep rate kinetics of the In–Sn–Pb–Cd solder were represented by Eq. 9 below:

$$\mathrm{d}\varepsilon/\mathrm{d}t_{\min} = 7.2 \times 10^6 \sinh^{2.1\pm0.3}(0.182\sigma)\exp(-66 \pm 7/RT) \tag{11}$$

The R^2 value for the regression analysis was 0.97 demonstrating an excellent correlation between the independent and dependent variables. The sinh law exponent was slightly higher than the values calculated for the In–Sn solder in Eqs. 8 and 9. Also, the apparent activation energy in Eq. 11 was still commensurate with a fast-diffusion mechanism.

A direct comparison was made of the steady-state creep rates between the as-fabricated conditions of the In–Sn solder [Eq. 8] and In–Sn–Pb–Cd alloy [equation (11)]. The corresponding plot was shown in Fig. 33. The In–Sn–Pb–Cd solder showed a slightly faster strain rate than the In–Sn solder. That difference increased with both test temperature as well as applied stress. These results corroborated the earlier analysis of creep strains, that the In–Sn solder was more creep resistant than its Pb-bearing counterpart.

In summary, the compression creep behaviors were evaluated for the low-melting temperature In–Sn and In–Sn–Pb–Cd solders. The In–Sn solder creep curves exhibited extensive tertiary stage behavior, which correlated with the development of cracking along coarsened cell boundaries. The annealing treatment had very little effect on either the strain-time behavior or the steady-state creep rate kinetics of the In–Sn solder. With the exception of creep at –25°C, the In–Sn solder was more creep resistant than was the In–Sn–Pb–Cd solder. The apparent activation energy indicated that the rate kinetics of creep for both solders was controlled by a fast diffusion mechanism.

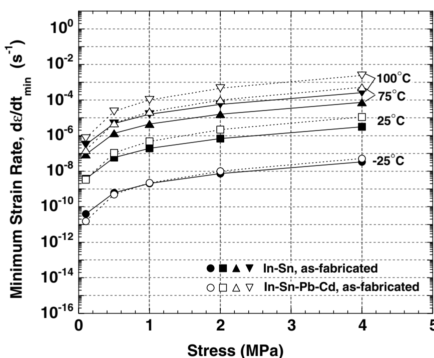

Fig. 33 Plot of the sinh law equations of steady-state creep strain rate comparing the In–Sn and In–Sn–Pb–Cd solders in the as-fabricated condition

4 Applications note

The creep and plastic deformation properties were evaluated for the two Pb-free solders, In–Ag and In–Sn. These two alloys represented melting temperature regimes that could be used to develop a step-soldering process for the assembly of OE, MEMS, and MOEMS devices. Several *qualitative* comparisons were made with respect to relative abilities of the Pb-free solders to deform when compared to the Pb-bearing counterpart alloy—e.g., for relieving residual stresses. In the case of the In–Ag and In–Pb–Ag solders, a comparison of creep and plastic deformation properties indicated that, in general, the In–Ag solder would deform to a greater degree than the In–Pb–Ag solder. On the other hand, the In–Sn solder had the lesser capacity to deform under an applied load versus the In–Sn–Pb–Cd material.

Nevertheless, it has been recognized that, in most applications, both plastic and creep deformation can occur to varying degrees. Secondly, it is necessary to have a *quantitative* prediction of the ensuing deformation for engineering design and reliability analyses as would be provided by the single UCP constitutive model. Therefore, a long-range goal is to develop a UCP constitutive model for each of the Pb-free solders that would form the basis of a TMF predictive (numerical) model. Of course, the UCP constitutive equation would describe the deformation leading up to crack initiation, only. At this stage, the equation would not be capable of describing damage in the form of crack propagation.

The associated constitutive equations were developed for the In–Ag solder, representing both the as-fabricated and annealed conditions. This as-fabricated case will be highlighted below. The one-dimensional equation for the inelastic strain rate in the UCP model is:

$$\mathrm{d}e/\mathrm{d}t_{11} = f_0\{\sinh^p[(|\sigma_{11} - B_{11}|/\alpha D]\}(\sigma_{11} - B_{11})\exp(-{}^{\cdot}H/RT) \tag{12}$$

where the subscript (11) denotes the uniaxial compression direction; B_{11} is the directional hardening which, at this point in the study, was taken to be a constant; and D represents the internal state variable of isotropic hardening/recovery, which is described by

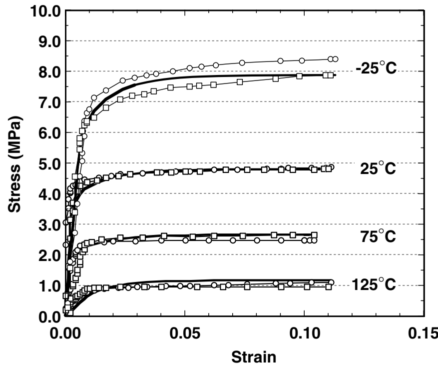

Fig. 34 Graph comparing the stress–strain behavior of the as-fabricated In–Ag solder at 4.4×10^{-5} s^{-1} (symbols) to the predictions calculated by the UCP constitutive model (solid lines)

$$dD/dt = \{[A_1|de/dt_{11}|]/[(D - D_0)^{A}_{3}]\} - A_2(D - D_0)^2 \quad (13)$$

where A_1, A_2, A_3, and D_0 are material constants. These material constants were initially constructed from the steady-state creep equation and then adjusted to calibrate the model prediction with both creep and plastic deformation experimental data. Thus, in Eq. 12, the values of f_0, α, p, and $\dot{H}$ were the same as those determined in Eq. 4, except that the value of α used in Eq. 12 was approximated to 1.0.

The prediction capability of Eq. 12, when populated with the suitable parameters, was assessed using the stress-stain behavior of the In–Ag solder. Shown in Fig. 34 is a plot that shows the two experimental stress–strain curves (symbols) for the as-fabricated In–Ag solder per each test temperature. The strain rate was 4.4×10^{-5} s^{-1}. The model prediction was represented by the solid lines. The UCP model adequately represented the plastic deformation. Similar correlations were observed at the faster strain rate as well as for both strain rates after the In–Ag solder in the annealed condition. Therefore, Eqs. 12 and 13 would be suitable for the UCP constitutive model in a finite element computational model for predicting the deformation behavior of In–Ag in a solder joint.

5 Summary

1. Lead (Pb)-free, low melting temperature solders are required for the step-soldering process used to assemble complex micro-electrical mechanical system (MEMS), OE, and micro-optical, electrical, mechanical system (MOEMS) devices. Stringent alignment protocols as well as the long-term stability of component placement necessitate the use of computational models to predict solder deformation following the assembly process as well as in response to anticipated service conditions.
2. The development of suitable computational models for such solder joints, begins with constructing a UCP constitutive model that describes both plastic and creep deformation properties of the solder alloy.
3. The stress–strain and creep properties were measured for the low-temperature, Pb-free 97In-3Ag (wt.%) and 58In-42Sn solders using compression testing techniques. The companion, Pb-bearing solders, 80In–15Pb–5Ag and 70In–15Sn–9.6Pb–5.4Cd, respectively, were similarly tested for comparison purposes.
4. Compression stress–strain tests were performed at strain rates of 4.4×10^{-5} s^{-1} and 8.8×10^{-4} s^{-1} and temperatures of –25, 25, 75, and 100°C or 125°C. Compression creep tests were performed at the same four temperatures. The minimum strain rate at the steady-state creep stage was represented by the equation: $f_0 \sinh^p (\alpha\sigma) \exp(-\Delta H/RT)$. Samples were evaluated in the as-fabricated (cast) condition and after thermal annealing.
5. The stress–strain plots of the In–Ag solder exhibited reduced strain hardening with increased test temperature. The yield stress values were in the range of 0.5 MPa to 8.5 MPa and decreased with both test temperature and strain rate. The yield stresses were sensitive to the annealing treatments only at –25 and 25°C. The static elastic modulus generally decreased with test temperature, although not in a monotonic manner.
6. The values of ΔH for steady-state creep were 99 ± 14 kJ/mol and 46 ± 11 kJ/mol, indicating that bulk diffusion controlled creep in the as-fabricated samples and fast-diffusion controlled creep of the annealed samples, respectively.
7. The stress–strain plots of the In–Sn solder showed strain softening that resulted from dynamic recovery/recrystallization process. The yield stress ranged from 1.0 MPa to 22 MPa and decreased with both test temperature and strain rate. The annealing treatments did not significantly nor consistently change the yield stress. Two temperature regimes distinguished the static elastic modulus values.

8. The values of ΔH for steady-state creep were 55 ± 11 kJ/mol and 48 ± 13 kJ/mol for the as-fabricated and annealed conditions, respectively, indicating that fast diffusion, was the controlling mechanism in both cases.
9. UCP constitutive models were derived for the In–Ag solder representing the as-fabricated and 67°C, 16 h annealing conditions. The respective UCP equations represented very well the stress–strain behavior of the solder at both strain rates.

Acknowledgments The authors wish to thank A. Kilgo with assistance in metallographic sample preparation, M. Dvorack for his thorough review of the manuscript, and the US Army, Redstone Arsenal, AL for their financial support of this study.

References

1. T. Massalski (ed.), *Binary Alloy Phase Diagrams* (ASM, International, Materials Park, OH; 1986); vol. 1, p. 34 and vol. 2, p. 1401.
2. Z. Mei, J. Morris, J. Electron. Mater. **21**, 401 (1992)
3. J. Goldstein, J. Morris, J. Electron. Mater. **23**, 477 (1994)
4. J. Hwang, R. Vargas, Solder Surface Mount Technol. **5**, 38 (1990)
5. J. Seyyed, Solder Surface Mount Technol. **13**, 26 (1993)
6. F. Garofalo, *Fundamentals of Creep and Creep Rupture in Metals* (MacMillian, New York, NY, 1965), p. 156
7. A. Krausz, H. Eyring, *Deformation Kinetics* (McGraw-Hill, New York, NY), p. 190
8. F. Garofalo, op. cit., p. 25
9. P. Vianco, J. Rejent, A. Kilgo, J. Electron. Mater. **32**, 142 (2003)
10. P. Vianco, J. Rejent, A. Kilgo, J. Electron. Mater. **33**, 1389 (2004)
11. G. Dieter, *Mechanical Metallurgy* (McGraw-Hill, New York, NY, 1976), p. 75
12. Standard Test Methods for Young's Modulus, Tangent Modulus, and Chord Modulus, *ASTM E111–82* (American Society for Testing and Materials, West Conshohocken, 1995)
13. O. Sherby, P. Burke, Progress Mater. Sci. **13**, 340 (1968)
14. J. Stephens, D. Frear, Metall. Mater. Trans. A **30A**, 1301 (1999)
15. *Solder Alloy Data–Mechanical Properties of Solders and Soldered Joints* Report 656 (Inter. Tin Research Institute, Uxbridge, Middlesex, UK, 1986), pp. 12, 38
16. D. Shangguan (ed.), *Lead-Free Solder Interconnect Reliability* (ASM, Inter., Materials Park, 2005), p. 67
17. J. Askin, *Tracer Diffusion Data* (Plenum, New York, 1970)
18. *Smithells Metal Reference Book*, 6th edn. (Butterworth and Co. New York, 1983) pp. 13–18
19. P. Shewmon, *Diffusion in Solids*, 2nd edn. (TMS, Warrendale, 1989), p. 197
20. P. Shewmon, *Transformations in Metals* (McGraw-Hill, New York, NY, 1969), p. 61
21. J. Christian, *The Theory of Transformations in Metals and Alloys: Part I–Equilibrium and General* (Pergamon, Oxford, UK, 1975), p. 411